Structural, Vibrational, and Electronic Study of α-As$_2$Te$_3$ under Compression

V.P. Cuenca-Gotor,[1] J.A. Sans,[1,*] J. Ibáñez,[2] C. Popescu,[3] O.Gomis,[4] R. Vilaplana,[4] F.J. Manjón,[1] A. Leonardo,[5,6] E. Sagasta,[7] A. Suárez-Alcubilla,[8,9] I.G. Gurtubay,[6,8] M. Mollar,[1] and A. Bergara[6,8,9]

1 Instituto de Diseño para la Fabricación y Producción Automatizada, Universitat Politècnica de València, 46022 Valencia (Spain)

2 Institut de Ciències de la Terra Jaume Almera, CSIC, Barcelona (Spain)

3 ALBA-CELLS, 08290 Cerdanyola, Barcelona (Spain)

4 Centro de Tecnologías Físicas, Universitat Politècnica de València, 46022 Valencia (Spain)

5 Dpto. de Física Aplicada II, Universidad del País Vasco, UPV/EHU, 48080 Bilbao (Spain)

6 Donostia International Physics Center (DIPC), 20018 Donostia (Spain)

7 CIC NanoGUNE, E-20018, Donostia, San Sebastián (Spain)

8 Dpto. de Física de la Materia Condensada, Universidad del País Vasco, UPV/EHU, 48080 Bilbao (Spain)

9 Centro de Física de Materiales CFM, Centro Mixto CSIC-UPV/EHU, 20018 Donostia (Spain)

ABSTRACT We report a study of the structural, vibrational, and electronic properties of layered monoclinic arsenic telluride (α-As$_2$Te$_3$) at high pressures. Powder x-ray diffraction and Raman scattering measurements up to 17 GPa have been complemented with *ab initio* total-energy, lattice dynamics, and electronic band structure calculations. Our measurements, which include previously unreported Raman scattering measurements for crystalline α-As$_2$Te$_3$, show that this compound undergoes a reversible phase transition above 14 GPa at room temperature. The monoclinic crystalline structure of α-As$_2$Te$_3$ and its behavior under compression are analysed by means of the compressibility tensor. Major structural and vibrational changes are observed in the range between 2 and 4 GPa and can be ascribed to the strengthening of interlayer bonds. No evidence of any isostructural phase transition has been observed in α-As$_2$Te$_3$. A comparison with other group-15 sesquichalcogenides allows understanding the structure of α-As$_2$Te$_3$ and its behavior under compression based on the activity of the cation lone electron pair in these compounds. Finally, our electronic band structure calculations show that α-As$_2$Te$_3$ is a semiconductor at 1 atm, which undergoes a trivial semiconducting-metal transition above 4 GPa. The absence of a pressure-induced electronic topological transition in α-As$_2$Te$_3$ is discussed.

INTRODUCTION

Arsenic telluride (As$_2$Te$_3$) and other group-15 sesquichalcogenides with generic formula A_2X_3 (*A*=As, Sb, Bi; *X*= S, Se, Te) have been widely studied because of their outstanding thermoelectric properties[1-3]. In this regard, the most stable phase of arsenic telluride at ambient conditions (α-As$_2$Te$_3$) is a layered structure with monoclinic *C2/m* symmetry[4-6] and a smaller figure of merit than Sb- and Bi-based tellurides[7]; however, the metastable β-As$_2$Te$_3$ polymorph, known for many years[8-11] and with layered tetradymite-like rhombohedral *R-3m* symmetry,

exhibits notable thermoelectric properties[12,13]. Additionally, As_2Te_3 glasses have also been extensively studied due to their interesting applications as IR devices, electric and optical switches, memory devices, high-resolution displays, acousto-optic devices, optical fibers and amplifiers[14-19].

The recent discovery of 3D topological insulators (TIs) among group-15 sesquichalcogenides[20-22] has stimulated in the last years the study of these materials, which crystallize in a number of polymorphs depending on the activity of the cation lone electron pair (LEP). Many of the group-15 sesquichalcogenides that behave as 3D TIs crystallize in the layered tetradymite *R-3m* structure, like α-Sb_2Te_3, α-Bi_2Se_3 and α-Bi_2Te_3. Since this phase has been found in several sesquichalcogenides at high pressures (HP) and/or high temperatures (HT), HP studies of these materials are extremely interesting in order to search for new 3D TIs. Consequently, a number of HP experimental and theoretical studies have been conducted in recent years in group-15 sesquichalcogenides looking for an improvement of thermoelectrical properties or for the discovery of topological properties[23-43] (see Ref. 23 for studies prior to 2013).

Despite the interest in group-15 sesquichalcogenides from both fundamental and technological points of view, many properties of crystalline As_2Te_3 are unknown. In particular, there is no report on the vibrational properties of crystalline phases of As_2Te_3 even at room conditions up to our knowledge and only a few HP studies have been devoted to crystalline As_2Te_3. In this respect, synthesis at HP/HT conditions explored the phase boundary between the α and β phases up to 2 GPa three decades ago[8,9] and much later, changes in the thermoelectric power of α-As_2Te_3 were reported above 2 and 6 GPa and a structural transformation to β-As_2Te_3 between 6 and 8 GPa was claimed without reporting full structural details of the high-pressure phase[7].

Finally, two recent studies of α-As$_2$Te$_3$ up to 40 and 47 GPa have been reported. In these two works, two isostructural phase transitions (IPTs) of α-As$_2$Te$_3$ and a progressive first-order phase transition to the γ-Bi$_2$Te$_3$ phase above 13-15 GPa have been reported[42,43]. In this regard, it must be noted that a new monoclinic $P2_1/m$ (named β') has also been recently found at low temperatures[44].

As regards the electronic structure, recent *ab initio* calculations have reported that uniaxially-strained β-As$_2$Te$_3$ should undergo a pressure-induced electronic topological transition (ETT) leading from a trivial insulator to a Weyl semimetal and then to a topological insulator[45]. On the other hand, a recent work has reported electrical measurements at HP combined with theoretical *ab initio* calculations and observed the metallization of α-As$_2$Te$_3$ above 5 GPa[42]; however, another recent work has suggested on the basis of theoretical calculations that there is no metallization of α-As$_2$Te$_3$ on increasing pressure but two second-order electronic transitions[43]. These recent studies contrast with previous studies of amorphous and liquid semiconductors As$_2$S$_3$, As$_2$Se$_3$ and As$_2$Te$_3$ at HP that suggested a decrease of the optical and electronic bandgap with increasing pressure, leading to a common semiconductor-metal transition and glass transitions[46-52].

On the light of the cited works and the interesting properties found in other group-15 sesquioxides and sesquichalcogenides, it is interesting to study the properties of α-As$_2$Te$_3$ at HP in order to: i) understand the stability of their different polymorphs; ii) check if there is any IPT or ETT in α-As$_2$Te$_3$; iii) verify if α-As$_2$Te$_3$ undergoes metallization under compression; and iv) explore if α-As$_2$Te$_3$ can behave as a 3D-TI at HP. For those reasons, here we report a HP study of structural, vibrational, and electronic properties of α-As$_2$Te$_3$ at room temperature by means of powder x-ray diffraction (XRD) and Raman scattering (RS) measurements up to 17 GPa, which

are complemented with *ab initio* total energy, lattice dynamics and electronic structure calculations. We will show that our measurements show a reversible phase transition above 14 GPa to the γ phase in good agreement with a recent reports[42,43], but no IPTs are found in α-As_2Te_3 contrary to the same recent reports[42,43]. The crystalline structure and compressibility of α-As_2Te_3 is analysed by calculating the compressibility tensor at HP and explained on the light of its comparison to that of other group-15 sesquichalcogenides by taking into account the activity of the cation LEP. The RS spectrum of α-As_2Te_3 at room conditions is reported for the first time and its HP behaviour has been discussed. Finally, our electronic band structure calculations suggest that there is a progressive closing of the bandgap of α-As_2Te_3 with increasing pressure leading from a trivial semiconductor to a trivial metal above 4 GPa with no evidence for a pressure-induced ETT. Taking into account that the calculated bandgap is slightly underestimated in our calculations, we suggest the closing of the experimental bandgap above 5-6 GPa in good agreement with a recent work[42], but in disagreement with another recent study[43]. Therefore, our results are consistent with the changes in resistivity and thermopower measurements previously reported[7,42].

EXPERIMENTAL DETAILS

Commercially available polycrystalline As_2Te_3 powder (Alfa-Aesar, 99.999%) was used in the present study. XRD measurements at ambient pressure performed with a Rigaku Ultima IV diffractometer showed that samples correspond to the α phase with no presence of other phases or impurities. HP angle-dispersive powder XRD experiments at room temperature up to 17 GPa were conducted in a membrane-type diamond anvil cell (DAC) at the BL04-MSPD beamline of ALBA synchrotron. Incident monochromatic beam with wavelength of 0.4246 Å was focused to 20 x 20 μm using a pinhole of 50 μm to cut the x-ray beam tail[53]. Images covering a 2θ range up

to 18° were collected using a SX165 CCD located at 240 mm from sample. One-dimensional diffraction profiles of intensity as a function of 2θ were obtained by integration of the observed intensities with the Fit2D software[54]. Rietveld refinement of the experimental diffraction patterns gave reliable correlation factors up to 6 GPa. Above this pressure, the atomic positions have not been included in the fit and the lattice parameters were extracted through a Le Bail analysis of the experimental diffraction patterns. Rietveld and Le Bail refinements were carried out with GSAS package software for synchrotron measurements[55,56]. Interatomic distances were extracted with VESTA software[57]. The equation of state (EoS) of copper[58], whose powder was mixed with the sample powder, was used for pressure calibration.

Room-temperature unpolarized RS measurements up to 12 GPa were carried out with a Horiba Jobin Yvon LabRAM HR spectrometer equipped with a thermoelectrically cooled multichannel CCD detector that enables a spectral resolution better than 2 cm^{-1}. RS measurements were excited using the 6328-Å line of a He:Ne laser with an output power below 0.3 mW in order to avoid laser heating since these samples are very prone to laser damage both outside and inside the DAC. This fact could explain why RS measurements even at ambient conditions have not been previously reported for this compound to our knowledge. Pressure was determined with the ruby fluorescence method[59]. In both HP-XRD and HP-RS measurements, methanol-ethanol (4:1 ratio) mixture was used as a pressure-transmitting medium with hydrostatic conditions up to 10 GPa and quasi-hydrostatic conditions up to 17 GPa[60,61].

THEORETICAL DETAILS

Ab initio total-energy calculations were performed for α-As$_2$Te$_3$ and β-As$_2$Te$_3$ within the density functional theory (DFT)[62] using the plane-wave method and the pseudopotential theory with the Vienna Ab initio Simulation Package (VASP)[63] including scalar relativistic effects and spin-orbit

interaction (SOI). The projector-augmented wave scheme (PAW)[64-67] was used as implemented in this package and the basis set of plane waves extended up to an energy cutoff of 440 eV in order to achieve highly converged results and accurate description of the electronic properties. The exchange-correlation energy was described in the generalized gradient approximation (GGA) with the PBE prescription[68]. In order to obtain very well converged energies and forces, the integration over the Brillouin zone (BZ) was performed using dense meshes of special k-points. At selected volumes, the structures were fully relaxed to their optimized configuration through the calculation of the forces on atoms and the stress tensor. In the optimized configurations, the forces on the atoms are less than 0.002 eV/Å and the deviations of the stress tensor from a diagonal hydrostatic form are less than 1 kbar (0.1 GPa).

Electronic band-structure calculations were carried out at different pressures along selected paths on the first BZ. In turn, lattice-dynamics calculations were performed at the zone center (Γ point) and along high-symmetry directions of the BZ as a function of pressure using the direct-force constant approach[69]. The construction of the dynamical matrix at the Γ point of the BZ involves separate calculations of the forces that result from a fixed displacement away from equilibrium of the atoms in the primitive cell. The diagonalization of the dynamical matrix provides the normal-mode frequencies. Moreover, these calculations allow identifying the irreducible representations and the character of the vibrational phonon modes at the Γ point.

RESULTS AND DISCUSSION

Structural and vibrational characterization of α-As$_2$Te$_3$ at room conditions

As$_2$Te$_3$ usually crystallizes in the α polymorph with monoclinic *C2/m* space group. The crystalline structure of the α phase (Fig. 1) is composed of zigzag layers piled up mainly along

the *a* axis, which are linked by very weak van der Waals forces. In turn, zigzag layers are formed by rods extending along the *b* axis, which are linked by weak ionic-covalent As-Te forces mainly along the *c* axis. This zigzag layered structure is similar to that recently described for Sb_2S_3, Sb_2Se_3, and Bi_2S_3[41]. In α-As_2Te_3, there are five atoms occupying independent *4i* Wyckoff sites (As1, As2, Te1, Te2 and Te3); i.e., all atoms are located in the planes *y*=0 and *y* =1/2. The two independent As1 and As2 atoms have fivefold and sixfold coordination, respectively. In particular, Te atoms around As2 form a distorted octahedron with As-Te distances around 2.8 Å, while Te atoms around As1 form a square-based pyramid in a 3+2 coordination with three As-Te distances around 2.7 Å and two distances around 3.2 Å. This fivefold and sixfold coordination of As atoms in α-As_2Te_3 contrasts with the pure sixfold coordination of As atoms in β-As_2Te_3. In this regard, we must note that a higher 5+2 coordination has been proposed for As1 in α-As_2Te_3 (with two long (> 4Å) As-Te distances between As1 atoms and Te atoms corresponding to the adjacent layer)[6]. We will show later in the discussion of HP-XRD results that the right coordination of As1 in α-As_2Te_3 at room conditions is five.

The experimental XRD pattern of our sample at ambient conditions (Figure 2a) can be refined with a Gd_2Cl_3-type structure (*C2/m* space group), with small residuals and a correlation factor R_{wp} of 10%, yielding the following lattice parameters: a = 14.3441(4) Å, b = 4.01627(19) Å, c = 9.8895(4) Å and β = 95.053(3)º with V_0 = 567.52(3) Å^3. These values show good agreement with our theoretical lattice parameters (see Table 1) and with previously reported experimental values[4-6,42,43]. Furthermore, our theoretical values at room pressure compare also well to those of recently reported *ab initio* calculations including SOI[70]. Therefore, our XRD analysis at room conditions shows that our sample corresponds to pure α-As_2Te_3. No traces of crystalline Te have been observed in our samples.

As regards the vibrational properties of α-As$_2$Te$_3$, group theory predicts thirty zone-center vibrational modes at the BZ center with mechanical representation[71]:

$$\Gamma_{30} = 10(A_g + B_u) + 5(A_u + B_g) \qquad (1)$$

where g (gerade) modes are Raman active and u (ungerade) modes are infrared (IR) active, except one A_u and two B_u modes, which are acoustic modes. Therefore, α-As$_2$Te$_3$ has 15 Raman-active modes and 12 IR-active modes. A_u and B_g modes correspond to atom vibrations along the b-axis while A_g and B_u modes correspond to vibrations of atoms in the a-c plane.

Figure 2b shows unpolarized RS spectrum of α-As$_2$Te$_3$ at room conditions together with the theoretically predicted frequencies (bottom marks) scaled in intensity according to theoretical calculations of the Raman scattering cross section. The values of the experimental and theoretical frequencies of the Raman-active modes of α-As$_2$Te$_3$ at room pressure are summarized in Table 2. It can be observed that our RS spectrum clearly shows 10 out of the 15 Raman-active modes with a rather good agreement between our experimental and theoretical frequencies and intensities. However, the large number of Raman-active modes in a small frequency region of the RS spectrum at room pressure and the broadening of experimental peaks makes their identification, using only the RS spectrum at room pressure with the help of *ab initio* calculations, almost impossible. Therefore, a tentative assignment of experimental peaks has been performed on the basis of HP-RS measurements and calculations commented in a posterior section.

RS spectrum of α-As$_2$Te$_3$ is dominated by a mode close to 120 cm^{-1} and two characteristic high-frequency modes between 170 and 200 cm^{-1}. Unfortunately, our RS spectrum of crystalline

α-As$_2$Te$_3$ cannot be compared to previous measurements since this is the first time this RS spectrum is reported to the best of our knowledge. However, we must note that our RS spectrum is consistent with RS spectra reported in glasses containing As and Te (see discussion in the Supporting Information), which show vibrational frequencies[72-78] below 200 cm^{-1}. In this regard, it must be stressed that the RS spectrum of α-As$_2$Te$_3$ resembles that of crystalline Te since the most intense mode of the RS spectrum of α-As$_2$Te$_3$ (the A$_g^7$ mode around 120 cm^{-1}) occurs at a similar frequency as the most intense mode (A$_1$ mode) of crystalline Te[79]. We will show latter in our HP-RS study that the RS spectrum of α-As$_2$Te$_3$ at several pressures shows two Raman-active modes of crystalline Te: the A$_1$ mode of Te which is overlapped with the A$_g^7$ mode near 120 cm^{-1} and the E'' mode of Te around 140 cm^{-1} (marked with an asterisk in Fig. 2b). Since XRD peaks of crystalline Te do not appear in our XRD pattern at ambient conditions, laser heating appears to be responsible for the presence of these Te-related modes, even at the small powers used in this work for exciting RS measurements. Further discussion of the vibrational properties of α-As$_2$Te$_3$ is given in the Supporting Information, where four characteristic Raman-active modes have been discussed and visualized and with the J-ICE software (see **Fig. S1** in the Supporting Information)[80] in the same way as was previously reported for monoclinic α-Bi$_2$O$_3$[81].

HP-XRD measurements

Figure 3 shows powder HP-XRD patterns of α-As$_2$Te$_3$ at selected pressures up to 17.2 GPa. It can be observed that the low-pressure monoclinic *C2/m* structure is stable up to 14 GPa. Above this pressure, a reversible structural transition to a HP phase is evidenced by new peaks (marked by asterisks in Fig. 3) in the pattern of 17.2 GPa and by the recovery of the XRD pattern of α-As$_2$Te$_3$ on releasing pressure to room pressure (see pattern at the top of Fig. 3). This result is in agreement with two recent works[42,43], but contrasts with a previous work that reported a phase

transition to β-As_2Te_3 between 6 and 8 GPa under non-hydrostatic conditions[7]. None of the peaks of the new phase can be assigned either to β-As_2Te_3 nor to β'-As_2Te_3. Our XRD pattern at 17.2 GPa match with the γ-Bi_2Te_3 and γ-Bi_2Se_3 phases (monoclinic *C2/c*) phase in good agreement with the two recent works[42,43]. The study of the HP phase of α-As_2Te_3 is out of the scope of this work.

Rietveld refinements performed up to 6 GPa and Le Bail analysis at higher pressures (see examples in **Fig. S2** of the Supporting Information) allowed us to get the structural parameters of α-As_2Te_3 at different pressures. A monotonous decrease of the unit cell volume of α-As_2Te_3 up to 14 GPa is observed (**Fig. 4a**). Fit of pressure vs. experimental volume to a third-order Birch-Murnaghan equation of state (BM-EoS)[82] yields a zero-pressure volume, bulk modulus and pressure derivative of the bulk modulus of: V_0=579(4) Å^3, B_0=24(3) GPa and B_0'=7.9(9), respectively. The volume at zero pressure, V_0, obtained from the BM-EoS fit is similar, but slightly different to the value measured outside the DAC. This is a common fact noted in many experimental works when XRD measurements outside the DAC are performed with commercial equipment by using the $K_{\alpha 1}$ and $K_{\alpha 2}$ lines of Cu, whereas HP-XRD patterns are measured using synchrotron radiation[83]. In any case, both results are comparable with those of literature[4-6,42,43]. On the other hand, our bulk modulus and pressure derivative under hydrostatic conditions are similar to those recently reported (B_0= 26 GPa, B_0'=9.0) under quasi-hydrostatic conditions[42], but different to those recently reported (B_0= 38.4 GPa, B_0'=4.0 fixed) under hydrostatic conditions[43]. In this respect, we must note that all these results are comparable since fixing B_0' leads to an increase of B_0. In fact, it seems to be unreliable to fix the bulk modulus pressure derivative to 4 in order to fit the volume vs. pressure in highly compressible non-covalent compounds with a

large cation LEP activity, as it has been observed for structurally-related sesquichalcogenides Sb_2S_3, Sb_2Se_3, and Bi_2S_3 characterized by bulk modulus pressure derivatives[41] larger than 4.

It must be also stressed that our results from our experimental BM-EoS are in good agreement with our theoretical BM-EoS: V_0= 603.2(6) Å^3, B_0= 19.7(3) GPa and B_0'=8.1(4). The theoretical bulk modulus is slightly smaller than the experimental one, which can be explained by the overestimation of the theoretical volume at zero pressure in the GGA-PBE approximation. As expected, our experimental and theoretical values for the bulk modulus of the α phase are larger than those deduced for As_2Te_3 glass (~15 GPa) from ultrasonic measurements[48]. However, it must be noted that our bulk moduli are much smaller than the value recently reported (42.7 GPa) from elastic constant calculations on the basis of GGA-PBE calculations[70].

The lattice parameters of α-As_2Te_3 up to 16 GPa also show a monotonous and smooth decrease as pressure increases (Fig. 4b). The nice agreement of the theoretical behavior of volume and lattice parameters with experimental results gives support to the absence of a first-order phase transition between 6 and 8 GPa at room temperature under hydrostatic conditions, unlike assumed in a previous work[7] and in agreement with recent works[42,43]. Furthermore, the pressure dependence of our lattice parameters do not show evidence of anomalies in the region close to 13 GPa which could be indicative of any IPT as recently suggested[43]. In this regard, it is possible that the anomalous changes of correlated a and c parameters observed in literature[43] could be due to mistakes in the fit due to the mixture of the low and high-pressure phases coexisting above 13 GPa.

For completeness, the experimental and theoretical pressure dependence of the axial ratios of α-As_2Te_3 are shown in **Fig. S3** of the Supporting Information. As can be observed, there is a monotonous behavior of the experimental c/b axial ratio, which is well reproduced by our

calculations. On the other hand, the theoretical *a/b* and *a/c* axial ratios display a non-monotonic dependence showing changes in the region between 2 and 4 GPa. Our axial ratios are similar to those recently reported[42,43], but we have not observed the anomalies found at some pressures in these two last works. In some recent works, changes in the pressure dependence of the axial ratios of several group-15 sesquichalcogenides have been considered as a proof for the occurrence of a pressure-induced ETT[29,39,40] because a minimum of the *c/a* ratio was previously observed to be coincident with the occurrence of a pressure-induced ETT in α-Bi$_2$Se$_3$, α-Sb$_2$Te$_3$, and α-Bi$_2$Te$_3$[23]. However, this fact has been put into question in recent works[41,84] because the minimum of the *c/a* ratio can be originated by a change in the ratio of interlayer/intralayer forces, and it cannot be taken for granted that this change should be necessarily translated into a change in the electronic density of states near the Fermi level.

Inset of **Fig. 4b** shows a change of the slope of the β monoclinic angle (always perpendicular to the *b*-axis) above 4 GPa. This result implies that in α-As$_2$Te$_3$ the direction of the *a*-axis changes with pressure; i.e., assuming that the directions of both *b* and *c* axis remain constant. The departure of β from 90º indicates that the direction of maximum compressibility at room pressure is not exactly that of the *a*-axis; i.e., the main direction in which layers are piled up (see Fig. 1). The change in the slope of the β angle together with the change of the compressibility of the *a* axis (correlated with a change in the *a/b* ratio) near 4-5 GPa has been interpreted in a recent work as a proof of the occurrence of a second-order IPT[42]. Similarly, changes of the β angle together with the changes in the electronic band structure near 3 and 6 GPa have been interpreted in a recent work as a proof of the occurrence of two second-order IPTs[43]. In the following we will demonstrate that no pressure-induced IPT occurs in α-As$_2$Te$_3$ up to the first-order phase

transition above 14 GPa; however, we will first analyse the compressibility tensor of our monoclinic material.

In order to evaluate the change in the direction of maximum compressibility as a function of pressure we have calculated and diagonalized the experimental and theoretical isothermal compressibility tensor, β_{ij}, at different pressures (details are given in the Supporting Information). This tensor is a symmetric second rank tensor which relates the state of strain of a crystal to the change in pressure that induced it[85] and it has been obtained with the finite Eulerian approximation as implemented in the Win_Strain package[86]. Diagonalization of the β_{ij} tensor at room pressure yields for our experiments the maximum, intermediate and minimum compressibilities $27.3(21) \cdot 10^{-3}$, $14.0(11) \cdot 10^{-3}$ and $4.7(4) \cdot 10^{-3}$ GPa^{-1}, respectively; whereas for the case of our calculations the obtained values for the compressibilities are $38(3) \cdot 10^{-3}$, $14.6 (11) \cdot 10^{-3}$ and $4.3(5) \cdot 10^{-3}$ GPa^{-1}. As observed, the a axis is the most compressible one, the b axis is by far the less compressible axis, and the compressibility of the c axis is intermediate between that of the a and b axes. The experimental (theoretical) axial compressibilities indicate that around 59% (67%) of the total compression at room pressure is being accommodated along the direction of maximum compressibility. The major compression direction at room pressure occurs in the (0 1 0) plane at the given angle ψ (see **Tables S1 and S2** in the Supporting Information) relative to the c-axis (from c to a) or equivalently at an angle θ relative to the a-axis (from a to c). In particular, the experimental major compression direction at room pressure is at $\theta = 16.0(1.4)^{\circ}$ from the a-axis whereas our calculations predict that it is at $5.5(7)^{\circ}$ from the a-axis (see red arrow in **Fig. 1b**).

As regards the behaviour of the compressibility tensor at HP, the evolution under pressure of the β_{xx} tensor coefficients (related to the axial compressibilities) are shown in **Fig. S4**. Note that

the evolution of the experimental and theoretical compressibility tensors at HP is very similar. The most notable feature is that the experimental compressibility of the *a* axis is higher than that of the *c* axis ($\beta_{11} > \beta_{33}$) below 2.0 GPa; however, both compressibilities are similar at 2 GPa and $\beta_{11} < \beta_{33}$ beyond 3 GPa within experimental uncertainties. Moreover, the decrease of the compressibility of the *a* axis with increasing pressure is so large that the compressibilities of the *a* and *b* axes become equal around 13 GPa ($\beta_{11} = \beta_{22}$). These results imply that the *c* axis becomes more compressible than the *a* axis above 3 GPa. In this way, the direction of maximum compressibility move away the *a* axis and approaches the *c* axis with increasing pressure; i.e., the θ angle increases. At 3 GPa the direction of maximum compressibility is closer to the *c* axis than to the *a* axis and at pressures beyond 5 GPa the direction of maximum compressibility is already very close to the *c*-axis.

From the experimental and theoretical compressibility tensors at different pressures we can obtain the experimental and theoretical volume compressibility (trace of the tensor) at each pressure, which is plotted in **Fig. S5**. As observed, there is a continuous evolution of the compressibility as a function of pressure that cannot be attributed to the presence of pressure-induced second-order IPT. This result contrasts with the pressure-induced second-order IPTs suggested in recent works[42,43]. In this respect, an IPT near 5 GPa on the basis of a change of the β angle, a change in the slope of the compressibility at HP, and a change in the reduced pressure vs. the Eulerian strain (F-f) plot has been suggested[42]. We plot in the inset of Fig. 4a the F-f plot of our experiments and calculations. As observed, no change of the slope is observed when using the unit cell volume obtained from our fitted EoS. Therefore, our measurements and calculations do not support the existence of any IPT up to 14 GPa. In any case, we have to note that the results of the F-f plot are not very fiable because they are very sensitive to errors in the

volume at room pressure and the dispersion of data measured at HP, as already discussed regarding the structural behavior of α-Bi$_2$Se$_3$, a compound which shows a pressure-induced second-order phase transition[87]. Further support to the absence of pressure-induced second-order IPTs in α-As$_2$Te$_3$ is provided below.

In order to better understand the HP behavior of the structural parameters in α-As$_2$Te$_3$ previously described, we have studied the experimental and theoretical pressure dependence of the x and z atomic parameters of the Wyckoff positions for the five non-equivalent As (As1 and As2) and Te (Te1, Te2 and Te3) atoms (see **Fig. S6**) and the main interatomic distances (see **Figs. S7 to S10**). As can be seen in **Fig. S6**, all atomic parameters evolve in a monotonous way between ambient pressure and 14 GPa. This result means that all atomic positions are located at planes b = 0 and ½ (*y=0* or *y=½* atomic coordinate) at all pressures up to 14 GPa and that the changes of the atomic parameters do not show evidence for any phase transition up to 14 GPa. No increase or decrease of the symmetry of our theoretical atomic positions is observed in the whole pressure range studied unlike in the case of β-Bi$_2$O$_3$ where an increase of symmetry has been observed along the β–β' IPT[88]. Therefore, our theoretical calculations do not support the existence of any IPT in α-As$_2$Te$_3$.

Similarly, **Figs. S7 to S10** show an overall monotonous decrease of the experimental and theoretical As-Te, As-As and Te-Te distances as pressure increases. In general, there is a good agreement between the behavior of experimental and theoretical interatomic distances. Note that the values of the refined distances are of the same order as those theoretically calculated, which indicates that the refinement is correct; however, errors in Rietveld refinement positions propagate when calculating interatomic distances, especially with increasing pressure, which accounts for the differences between experimental and theoretical data. Therefore, in the

following the discussion of the evolution of interatomic distances with pressure is going to be based on the evolution of the theoretical distances, which have been calculated in the whole range of pressure from 1 atm to 14 GPa.

Regarding the coordination of As1 atoms in α-As$_2$Te$_3$, **Fig. S7** shows that As1 is fivefold (3+2) coordinated at room pressure if one considers all intralayer As-Te bonds; i.e., intrarod As-Te bonds below 3.0 Å and interrod bonds above 3.2 Å. At pressures above 6 GPa, As1 atoms can be considered to become fivefold coordinated (all intralayer As-Te bonds below 3.0 Å). On the other hand, As1 polyhedral units only tend towards a 5+2 coordination at pressures far from the stability range of the low-pressure phase if interlayer As1-Te1 distances (> 3.5 Å at 14 GPa) are considered. Regarding the coordination of As2 atoms, **Fig. S8** shows that As2 is sixfold coordinated at room pressure and all six As2-Te distances tend to similar values above 6-7 GPa, thus indicating a regularization of the distorted As2 octahedron on increasing pressure. Finally, **Figs. S9 and S10** show that intralayer and interlayer As-As and Te-Te distances show different behaviors under pressure. Intralayer distances show a small compression, while interlayer distances show a large contraction up to around 3-4 GPa and a considerable saturation above this pressure range. **Figures S7 to S10** allow us to understand the different compressibilities of *a*, *b* and *c* axes at HP. At room pressure, the *a* axis is considerably more compressible than *b* and *c* axes at room pressure, as it was expected from the strong initial compression of the weak van der Waals forces present in the space between adjacent layers that are piled up mainly along the *a* axis (Fig. 1a). This strong compression of the *a* axis below 3 GPa is related to the strong compressibility of interlayer Te-Te distances in this pressure range. On the contrary, the *b*-axis is the less compressible axis at any pressure because of strong intralayer As-Te covalent bonds (< 3.0 Å) which extend along the *b*-axis. Finally, the compressibility of the *c*-axis is intermediate

between that of the *a* and *b* axes because of the presence of long As1-Te2 distances (> 3.2 Å) at room pressure. On the other hand, interlayer Te-Te distances at pressures above 3-4 GPa decrease at a similar rate as intralayer Te-Te distances with the exception of Te2-Te2 distances which extend mainly along the *c* axis. This result evidences the hardening of interlayer bonds and explains why the *a* axis is no more the most compressible axis above this pressure range and why the most compressible axis approaches the *c* axis as pressure increases as evidenced from the analysis of the compressibility tensor.

To finish this section regarding the structural properties of α-As$_2$Te$_3$, it is interesting to compare the structure of α-As$_2$Te$_3$ and its pressure behavior with that of other group-15 sesquichalcogenides. This family of compounds crystallize in a number of distorted crystalline structures due to the activity of the cation LEP, which increases in the series Bi-Sb-As[89]. Therefore, the study of the behavior of the As LEP in α-As$_2$Te$_3$ at HP is crucial in order to understand the properties of this compound and other group-15 sesquichalcogenides under compression. **Figs. S11a and S12a** in the Supporting Information show the decrease of the volume of the different Te polyhedra around As1 and As2 atoms, respectively. As observed, a good agreement is obtained between experiment and theoretically simulated evolution of these polyhedral units. The decrease of the distortion index (**Figs. S11b and S12b**) show that these polyhedra become more regular with increasing pressure and evidences a decrease of the As LEP activity with increasing pressure, in good agreement with previous results in a number of Sb and Bi-related materials[29,41,88,90,91]. A comparison of the structure of α-As$_2$Te$_3$ with that of α-Sb$_2$Te$_3$, α-Bi$_2$Te$_3$ and orthorhombic Sb$_2$Se$_3$ (isostructural to Sb$_2$S$_3$ and Bi$_2$S$_3$) and their pressure dependences is provided in the Supporting Information taking into account the cation LEP activity. We can conclude that the structure of α-As$_2$Te$_3$ and its pressure behavior can be

understood as intermediate between that of α-Sb$_2$Te$_3$ and Sb$_2$Se$_3$ in good agreement with what is expected from the activity of cation LEP in group-15 sesquichalcogenides. In this way, the non-observation of a pressure-induced second-order IPT in α-As$_2$Te$_3$ is consistent with the fact that no IPT has also been found in Sb$_2$Se$_3$[28], Bi$_2$S$_3$[29], or Sb$_2$S$_3$[41] with a similar zigzag layered structure. We speculate that the reason for the lack of pressure-induced IPTs in these compounds is due to the large structural flexibility of orthorhombic and monoclinic structures (with many free atomic parameters) to accommodate changes in the cation LEP activity due to pressure, as compared to cubic, tetragonal, and rhombohedral structures of α-Sb$_2$O$_3$, β-Bi$_2$O$_3$ and α-Sb$_2$Te$_3$, respectively, which already show pressure-induced second-order IPTs[88,92,93].

In summary, the effect of pressure in the structure of α-As$_2$Te$_3$ is a progressive contraction of the interlayer space and a slight rotation of polyhedral units (see the main difference between the structure of α-As$_2$Te$_3$ at 1 atm and 14 GPa in Fig. 1b) that leads to an increase of the average coordination of As ions and to a decrease of the distortion of the polyhedral units around As ions (due to the decrease of the cation LEP), but without modifying the y parameter of the initial Wyckoff sites of the five non-equivalent atoms of the unit cell. No evidence for a pressure-induced IPT has been found in α-As$_2$Te$_3$.

HP-RS measurements

As already discussed, HP-XRD measurements at room temperature under quasi-hydrostatic conditions show no phase transition to the β phase neither above 8 nor above 14 GPa, unlike expected from previous results[7]. In order to clarify the stability of both α-As$_2$Te$_3$ and β-As$_2$Te$_3$ phases, we have performed *ab initio* calculations of the enthalpy vs. pressure for both phases (**Fig. S13** in the Supporting Information). Unlike previous calculations[42], our calculations

suggest that the α-to-β phase transition in As_2Te_3 could occur at relatively small pressures (>1 GPa). This means that perhaps, the α-to-β phase transition in As_2Te_3 is kinetically hindered at room temperature and at quasi-hydrostatic conditions by a high energy barrier. Therefore, some additional thermal energy is needed in order to overcome this energy barrier. This result is in agreement with experiments reporting the existence of β-As_2Te_3 at relatively low pressures and high temperatures[8-11]. In this regard, a possible transition above 6 GPa as previously suggested from thermopower measurements[7] and expected from extrapolation of experimental HP/HT data at relatively low pressures[8,9], could correspond to the non-hydrostatic conditions in Ref. 7 or to thermal activation at HP derived from the increase in temperature inherent to thermopower measurements. Additionally, it can be observed from **Fig. S13** that the enthalpy of the β phase is higher than that of the α phase above 15 GPa; therefore, our calculations show that the β phase is not a competitive phase at very HP as it was previously assumed. This may explain why we have observed a new phase above 14 GPa different to that of the β phase in good agreement with two recent works[42,43].

In order to study the possible effect of hydrostaticity on the appearance of the α-to-β phase transition we have conducted HP-RS measurements at both hydrostatic and non-hydrostatic conditions, which have been compared to lattice-dynamical calculations in order to better understand the HP behavior of α-As_2Te_3. Fig. 5 shows room-temperature RS spectra of α-As_2Te_3 at selected pressures under hydrostatic conditions up to 12 GPa. It can be observed that RS spectra clearly correspond to α-As_2Te_3 in this pressure range.

As already mentioned, it is very difficult to assign the features that show up in the room-pressure RS spectrum of α-As_2Te_3. However, it is possible to perform a tentative peak assignment by studying the behavior of the Raman-active peaks at HP in combination with the

results of lattice-dynamical calculations. Fig. 6 shows the pressure dependence of the experimental and theoretical Raman-active mode frequencies of α-As$_2$Te$_3$ measured up to 12 GPa under hydrostatic conditions. In general, theoretical frequencies of Raman-active modes do not show a simple monotonic behavior with increasing pressure. In fact, they show a complex behavior with crossings and anticrossings of modes with different and equal symmetries, respectively. This complex behavior is caused by the presence of 15 Raman-active modes in a small region between 50 and 200 cm^{-1} similar to that found in orthorhombic Sb$_2$S$_3$, Sb$_2$Se$_3$ and Bi$_2$S$_3$[41]. Apart from crossings and anticrossings already observed in related orthorhombic compounds Sb$_2$S$_3$, Sb$_2$Se$_3$ and Bi$_2$S$_3$[41], small changes in the pressure coefficient of some theoretical Raman-active modes have been observed in the range between 2 and 4 GPain α-As$_2$Te$_3$, which could be attributed to the strong changes in the interatomic distances around these pressures already commented in the previous section.

Despite the complex behavior observed in theoretical Raman-active modes, several experimental modes are found to show a behavior consistent with the theoretical ones. In particular, the two high-frequency theoretical Raman modes above 160 cm^{-1} show small negative pressure coefficients at room pressure in rather good agreement with the almost negligible pressure coefficient of our two highest-frequency modes. These small negative or even negligible pressure coefficients are consistent with the small or even negligible increase of the shorter intralayer As1-Te distances (**Fig. S7**) at low pressures. Therefore, tentative assignments of the experimental Raman-active modes of α-As$_2$Te$_3$ reported in Fig. 6 have been made by comparing the experimental and theoretical values of frequencies and pressure coefficients. The tentative assignments are summarized in Table 2.

As observed in Fig. 6, we have additionally observed two experimental Raman modes in the range from 120 to 145 cm^{-1} (see blue symbols in Fig. 6) whose frequency decreases with increasing pressure. The frequencies of these two modes are close to those previously reported for crystalline Te[79], as already commented. Furthermore, the negative pressure coefficients shown by these two modes is in agreement with those reported for crystalline Te[91,92,94,95]. Consequently, we have attributed the modes near 120 cm^{-1} and near 140 cm^{-1} to the A$_1$ and E'' (marked with an asterisk in Fig. 2b) modes of crystalline Te. In this regard, we have to note that Raman-active modes associated to Te have been already observed in non-stoichiometic samples of Bi$_2$Te$_3$ nanowires and were assigned to Te clusters in Te-rich regions in nanowires[96]. Furthermore, segregation of Se nanoclusters caused by laser-induced damage during HP-RS measurements has also been observed in several chalcogenides[97,98]. In our experiments, it is highly difficult to avoid such damage when performing experimental RS measurements, at least with the red He:Ne laser. These modes are no longer observed at pressures beyond 4-5 GPa likely because of the improvement in the thermal conductivity inside the DAC with increasing pressure likely due to the metallization of α-As$_2$Te$_3$ as commented in the next section.

Room-temperature HP-RS spectra and the pressure dependence of the Raman-active modes under non-hydrostatic conditions (without pressure transmitting medium) are shown in **Figs. S14 and S15** in the Supporting Information, respectively. As observed, no phase transition near 6-8 GPa is observed either under hydrostatic or under non-hydrostatic conditions, thus supporting the hypothesis that thermal activation at HP is needed in order to force the α-to-β phase transition in α-As$_2$Te$_3$ at relatively low pressures[8,9].

In order to check if there could be any pressure-induced second-order IPT in α-As$_2$Te$_3$, we have also studied the phonon dispersion curves theoretically calculated at different pressures up

to 14 GPa (see **Fig. S16** in the Supporting Information) since second-order IPTs must be related to the presence of a soft phonon mode according to Landau theory. As observed, there is no soft mode along the whole BZ at any pressure either in the range from 3 to 5 GPa or in the range from 6 to 13 GPa, unlike in β-Bi_2O_3[88]. Therefore, we can safely conclude that there is no pressure-induced IPT in α-As_2Te_3 up to 14 GPa, unlike recently reported[42,43].

Finally, we must mention that in order to check if there could be a possible occurrence of a pressure-induced ETT in α-As_2Te_3, we have also studied the pressure dependence of the linewidth for the most intense Raman-active modes in both HP-RS experiments under hydrostatic and non-hydrostatic conditions. We have found no major change on increasing pressure which could be indicative of a pressure-induced ETT in this compound. Only a small increase of the RS background is observed above 4 GPa which could be indicative of the progressive metallization of the material above this pressure as will be discussed in the next section.

Electronic band structure calculations

Taking into account that ETTs are very subtle transitions (they are $2^{1/2}$ transitions in Ehrenfest notation) whose occurrence could be difficult to evidence by XRD or RS measurements, we have performed *ab initio* band-structure calculations in α-As_2Te_3 at HP in order to identify possible changes of the band extrema that could be related to a pressure-induced ETT. We show in **Fig. 7** the electronic band structure at different pressures. As can be seen, the electronic structure at 0 GPa exhibits an indirect bandgap (theoretical value around 0.7 eV) with the conduction band minimum (CBM) located close to the L point of the BZ and three almost degenerate valence band maxima (VBM) located in different directions close to the A point of the BZ in good

agreement with recent calculations[42], but in disagreement with other calculations[43,70]. In any case, all reported theoretical DFT results for α-As$_2$Te$_3$ at 0 GPa underestimate the experimental bandgap value at room pressure, which is estimated to be experimentally between 0.82 and 0.92 eV[99,100].

The indirect bandgap progressively closes at HP in good agreement with recent results[42,43]. Around 1 GPa, our calculations show that the bandgap remains indirect with a value above 0.4 eV and that the CBM changes from the L point to the V point. No major changes occur in the electronic band structure above this pressure. Our calculations indicate that the indirect bandgap of α-As$_2$Te$_3$ closes completely around 4 GPa undergoing a pressure-induced trivial semiconductor-metal transition and no other major change occurs at higher pressures. Therefore, due to the underestimation of the theoretical bandgap in DFT calculations, it is reasonable to assume that the actual closing of the bandgap takes place at a slightly larger pressure (around 6-7 GPa). This closing could explain the anomalies observed in thermopower measurements in this pressure range[7] and is in good agreement with the recent electric measurements and theoretical calculations of a recent report[42]. However, our results are in disagreement with another recent report that suggests two indirect-to-direct crossovers that have been incorrectly interpreted as IPTs[43] and whose calculations do not allow to explain the electrical results recently obtained[42].

In summary, our theoretical electronic band structure calculations show that α-As$_2$Te$_3$ is a semiconductor with an indirect bandgap above 0.7 eV at room pressure, whose energy decreases with increasing pressure until it becomes a semimetal above 4-6 GPa. Only a change in the location of the CBM in the BZ is observed around 1 GPa which could lead to a pressure-induced ETT; however, the bandgap at this pressure is too high (probably above 0.5 eV) to result in a strong modification of the electronic density of states near the Fermi level. Therefore, we

conclude that there is no evidence for a pressure-induced ETT in α-As$_2$Te$_3$ and that changes in the resistance of α-As$_2$Te$_3$ measured by Scheidemantel et al.[7] between 1 and 2 GPa and above 6 GPa match with the changes in the electronic band structure here reported. However, on the light of present results and the discrepancies observed among the different calculations, we must say that more precise calculations including SOI should be performed to shed further light on the pressure dependence of the electronic band structure of α-As$_2$Te$_3$.

CONCLUSIONS

We have studied the structural, vibrational, and electronic properties of α-As$_2$Te$_3$ at room temperature and high pressure. We have observed that there is a stronger interlayer compressibility in α-As$_2$Te$_3$ than in α-Sb$_2$Te$_3$ and α-Bi$_2$Te$_3$, which can be explained due to the larger lone electron pair effect of As than Sb and Bi. In fact, we have shown that the structure of α-As$_2$Te$_3$ can be understood as an intermediate structure between that of Sb$_2$Se$_3$ and α-Sb$_2$Te$_3$. Strong changes in the monoclinic β angle and in the axial compressibilities are observed in the region between 2 and 4 GPa, which are related to the strengthening of the interlayer van der Waals bonds in this pressure range. This feature was demonstrated by the change of the direction of the maximum compressibility given by the analysis of the compressibility tensor. Furthermore, we have observed that polyhedral units around As cations in α-As$_2$Te$_3$ become more regular with increasing pressure and show a small rotation in order to accommodate pressure in a clear tendency to increase the coordination with increasing pressure of both non-equivalent As atoms. Our *ab initio* theoretical simulations predict that the β phase, where As atoms are in true sixfold coordination, is thermodynamically more stable than the α phase above 1 GPa. However, no phase transition to the β phase has been observed at ambient temperature

even above 17 GPa but a phase transition to the γ phase. The lack of observation of the phase transition from α-As$_2$Te$_3$ to β-As$_2$Te$_3$ at ambient temperature is likely because it is a highly reconstructive first-order phase transition, which can be frustrated due to the presence of a high kinetic energy barrier and lately hidden by the phase transition towards a γ polymorph.

Our Raman scattering measurements and lattice dynamics calculations support the stability of the α phase up to 12 GPa and show small changes in the region between 2 and 4 GPa, consistent with the progressive changes of the interatomic distances with increasing pressure. Phonon dispersion curves at different pressures do not show any soft mode which evidences a pressure-induced second-order IPT. Additionally, changes in the RS spectrum which could be indicative of a pressure-induced ETT have not been observed. This is in agreement with theoretical calculations of the electronic band structure, which show that α-As$_2$Te$_3$ is an indirect semiconductor with a bandgap above 0.7 eV and which shows a change of the conduction band minimum close to 1 GPa. A closing of the indirect bandgap occurs with increasing pressure, which suggests experimentally a semiconductor-to-metal transition above 6 GPa.

ASSOCIATED CONTENT

Supporting Information. Supporting Information provides an analysis of the vibrational properties of α-As$_2$Te$_3$ at ambient pressure and at high pressure under non-hydrostatic conditions. Besides, details of the structural evolution of compressed α-As$_2$Te$_3$, showing the evolution of the theoretical and experimental Wyckoff free coordinates, the interatomic distances

and the polyhedral distortion under pressure is provided. On the other hand, an extensive description of the experimental and theoretical isothermal compressibility tensor together with all the information extracted from it and the evolution of the calculated enthalpy of the α and β polymorph of As_2Te_3 vs pressure is given. This material is available free of charge via the Internet at http://pubs.acs.org.

AUTHOR INFORMATION

Corresponding Author

*(J.A. Sans) E-mail: juasant2@upv.es. Telephone: (+34) 963877000 ext.(75269).

Author Contributions

The manuscript was written through contributions of all authors. All authors have given approval to the final version of the manuscript.

ACKNOWLEDGMENT

REFERENCES

(1) Nolas, G.S.; Sharp, J.; Goldsmid, J. *Thermoelectrics*. Eds.; Springer: Berlin, 2001.

(2) Scherrer H.; Scherrer S. Thermoelectric Properties of Bismuth Antimony Telluride Solid Solutions. *Thermoelectrics Handbook: Macro to Nano.* Ed. D.M. Rowe, CRC Press: Boca Raton, FL, 2005.

(3) Stordeur, M. Valence Band Structure and the Thermoelectric Figure-of-Merit of $(Bi_{1-x}Sb_x)Te_3$ Crystals. CRC Handbook of Thermoelectrics, Ed. D.M. Rowe, CRC Press: Boca Raton, FL, 1995.

(4) Carron, G.J. The Crystal Structure and Powder Data for Arsenic Telluride. *Acta Cryst.* **1963**, *16*, 338-343.

(5) Kanishcheva, A.S.; Milhailov, Y.N.; Chernov, A.P. Refinement of the Crystal Structure of Arsenic Telluride As_2Te_3. *Inorg. Mater.* **1982**, *18*, 796-799.

(6) Stergiou, A.C.; Rentzeperis, P.J. Hydrothermal Growth and the Crystal Structure of Arsenic Telluride, As_2Te_3. Z. Kristallogr. **1985**, *172*, 139-145.

(7) Scheidemantel, T.J.; Meng, J.F.; Badding, J.V. Thermoelectric Power and Phase Transition of Polycrystalline As_2Te_3 under Pressure. *J. Phys. Chem. Solids* **2005**, *66*, 1744-1747.

(8) Yakushev, V.A.; Kirkinskii, V.A. New Polymorphic Modification of Arsenic Telluride, Produced at high Pressures. *Dokl. Akad. Nauk SSSR* **1969**, *186*, 882-884; idem, *Dokl. Phys. Chem.* **1986**, *186*, 369-371.

(9) Kirkinskii, V.A.; Yakushev, V.G. The System As-Te at high Pressures. *Izves. Akad. Nauk SSSR, Neorg. Mat.* **1974**, *10*, 1431-1435; idem, *Inorg. Mater.* **1974**, *10*, 1230-1233.

(10) Shu, H.W.; Jaulmes, S.; Flahaut, J. System As/1bTe - Obtention and Structural Study of a new Variety of As_2Te_3, Metastable. *Mat. Res. Bull.* **1986**, *21*, 1509-1514.

(11) Toscani, S.; Dugue, J.; Ollitrault, R.; Ceolin, R. Polymorphism of As_2Te_3: Structural Studies and Thermal behavior of Rhombohedral β-As_2Te_3. Thermochim. Acta, **1991**, *186*, 247-251.

(12) Scheidemantel, T.J.; Badding, J.V. Electronic Structure of β-As_2Te_3. *Solid State Commun.* **2003**, *127*, 667-670.

(13) Vaney, J.B.; Carreaud, J.; Delaizir, G.; Piarristeguy, A.; Morin, C.; Alleno, E.; Monnier, J.; Gonçalves, A.P.; Candolfi, C.; Dauscher, A. et al. High-Temperature Thermoelectric Properties of Sn-Doped β-As_2Te_3. *Adv. Electron. Mater.* **2015**, *1*, 1400008.

(14) Thornburg, D.D. Physical Properties of the $As_2(Se,Te)_3$ Glasses. *J. Electron. Mater.* **1973**, *2*, 495-532.

(15) Madan, A.; Show, M.P. The Physics and Application of Amorphous Semiconductors. Academic Press: Boston-San Diego, 1988.

(16) H.Y. Hwang, G. Lenz, M.E. Lines, R.E. Slusher, US Patent No 6.208.792 (2001).

(17) Aggarwal, I.D.; Sanghera, J.S. Development and Applications of Chalcogenide Glass Optical Fibers at nrl. *J. Optoelectron. Adv. Mater.* **2002**, *4*, 665-678.

(18) Kovanda, V.; Vicek, M.; Jain, H.J. Structure of As–Se and As–P–Se Glasses Studied by Raman Spectroscopy. *J. Non-Cryst. Sol.* **2003**, *326-327*, 88-92.

(19) Sanghera, J.S.; Aggarwal, I.D.; Shaw, L.B.; Florea, C.M.; Pureza, P.; Nguyen, V.G.; Kung, F.J. Nonlinear Properties of Chalcogenide Glass Fibers. *J. Optoelectron. Adv. Mater.* **2006**, *8*, 2148-2155.

(20) Chen, Y.L.; Analytis, J.G.; Chu, J.-H.; Liu, Z.K.; Mo, S.-K.; Qi, X.L.; Zhang, H.J.; Lu, D.H.; Dai, X.; Fang, Z. et al. Experimental Realization of a Three-Dimensional Topological Insulator, Bi_2Te_3. *Science* **2009**, *325*, 178-181.

(21) Zhang, H.; Liu, C.-X.; Qi, X.-L.; Dai, X.; Fang, Z.; Zhang, S.-C. Topological Insulators in Bi_2Se_3, Bi_2Te_3 and Sb_2Te_3 with a Single Dirac Cone on the Surface. *Nature Phys.* **2009**, *5*, 438-442.

(22) Hsieh, D.; Xia, Y.; Qian, D.; Wray, L.; Meier, F.; Dil, J.H.; Osterwalder, J.; Patthey, L.; Fedorov, A.V.; Lin, H. et al. Observation of Time-Reversal-Protected Single-Dirac-Cone Topological-Insulator State in Bi_2Te_3 and Sb_2Te_3. *Phys. Rev. Lett.* **2009**, *103*, 146401.

(23) Manjón, F.J.; Vilaplana, R.; Gomis, O.; Perez-Gonzalez, E.; Santamaria-Perez, D.; Marin-Borras, V.; Segura, A.; Gonzalez, J.; Rodriguez-Hernandez, P.; Muñoz, A. High-Pressure Studies of Topological Insulators Bi_2Se_3, Bi_2Te_3, and Sb_2Te_3. *Phys.Status Solidi B* **2013**, *250*, 669-676.

(24) Liu, G.T.; Zhu, L.; Ma, Y.M.; Lin, C.L.; Liu, J. Stabilization of 9/10-Fold Structure in Bismuth Selenide at High Pressures. *J. Phys. Chem. C* **2013**, *117*, 10045-10050.

(25) Zhao, J.; Liu, H.; Ehm, L.; Dong, D.; Chen, Z.; Gu, G. High-Pressure Phase Transitions, Amorphization, and Crystallization Behaviors in Bi_2Se_3. *J. Phys.: Condens. Matter* **2013**, *25*, 125602.

(26) Kirshenbaum, K.; Syers, P.S.; Hope, A.P.; Butch, N.P.; Jeffries, J.R.; Weir, S.T.; Hamlin, J.J.; Maple, M.B.; Vohra, Y.K.; Paglione, J. Pressure-Induced Unconventional Superconducting Phase in the Topological Insulator Bi_2Se_3. *Phys. Rev. Lett.* **2013**, *111*, 087001.

(27) Zhu, J.; Zhang, J.L.; Kong, P.P.; Zhang, S.J.; Yu, X.H.; Zhu, J.L.; Liu, Q.Q.; Li, X.; Yu, R.C.; Ahuja, R. Superconductivity in Topological Insulator Sb_2Te_3 Induced by Pressure. *Sci. Rep.* **2013**, *3*, 2016.

(28) Efthimiopoulos, I.; Zhang, J.M.; Kucway, M.; Park, C.; Ewing, R.C.; Wang, Y. Sb_2Se_3 under Pressure. *Sci. Rep.* **2013**, *3*, 2665.

(29) Efthimiopoulos, I.; Kemichick, J.; Zhou, X.; Khare, S.V.; Ikuta, D.; Wang, Y. High-Pressure Studies of Bi_2S_3. *J. Phys. Chem. A* **2014**, *118*, 1713-1720.

(30) Zhang, J.K.; Han, Y.H.; Liu, C.L.; Zhang, X.; Ke, F.; Peng, G.; Ma, Y.M.; Ma, Y.Z.; Gao, C.X. Semiconductor-to-metal Transition of Bi_2Se_3 under High Pressure. *Appl. Phys. Lett.* **2014**, *105*, 062102.

(31) Kong, P.P.; Sun, F.; Xing, L.Y.; Zhu, J.; Zhang, S.J.; Li, W.M.; Liu, Q.Q.; Wang, X.C.; Feng, S.M.; Yu, X.H. Superconductivity in Strong Spin Orbital Coupling Compound Sb_2Se_3. *Sci. Rep.* **2014**, *4*, 6679.

(32) Brazhkin, V.V.; Orlov, A.I. High-Pressure Thermoelectric Characteristics of Bi_2Te_3 Semiconductor with Different Charge Carrier Densities. *JETP Lett.* **2014**, *99*, 283-285.

(33) Zhao, K.; Wang, Y.; Sui, Y.; Xin, C.; Wang, X.J.; Wang, Y.; Liu, Z.G.; Li, B.S. First Principles Study of Isostructural Phase Transition in Sb_2Te_3 under High Pressure. *Phys. Stat. Sol. RRL* **2015**, *9*, 379-383.

(34) Nielsen, M.B.; Parisiades, P.; Madsen, S.R.; Bremholm, M. High-Pressure Phase Transitions in Ordered and Disordered Bi_2Te_2Se. *Dalton Transactions* **2015**, *44*, 14077-14084.

(35) Wang, B.T.; Souvatzis, P.; Eriksson, O.; Zhang, P. Lattice Dynamics and Chemical Bonding in Sb_2Te_3 from First-Principles Calculations. *J. Chem. Phys.* **2015**, *142*, 174702.

(36) Ovsyannikov, S.V.; Morozova, N.V.; Korobeinikov, I.V.; Lukyanova, L.N.; Manakov, A.Y.; Likhacheva, A.Y.; Ancharov, A.I.; Vokhmyanin, A.P.; Berger, I.F.; Usov, O.A. et al. Enhanced Power Factor and High-Pressure Effects in $(Bi,Sb)_2(Te,Se)_3$ Thermoelectrics. *Appl. Phys. Lett.* **2015**, *106*, 143901.

(37) Yu, Z.H.; Wang, L.; Hu, Q.Y.; Zhao, J.G.; Yan, S.; Yang, K.; Sinogeikin, S.; Gu, G.; Mao, H.-K. Structural Phase Transitions in Bi_2Se_3 under High Pressure. *Sci. Rep.* **2015**, *5*, 15939.

(38) Zhang, H.Y.; Cheng, Y.; Tang, M.; Chen, X.R. Ji, G.F. First-Principles Study of Structural, Elastic, Electronic and Thermodynamic Properties of Topological Insulator Sb_2Te_3 under Pressure. *Comp. Mat. Sci.* **2015**, *96*, 342-347.

(39) Sorb, Y.A.; Rajaji, V.; Malavi, P. S.; Subbarao, U.; Halappa, P.; Peter, S. C.; Karmakar, S.; and Narayana, C. Pressure-Induced Electronic Topological Transition in Sb_2S_3. *J. Phys.: Condens. Mat.* **2016**, *28*, 015602.

(40) Efthimiopoulos, I.; Buchan, C.; Wang, Y. Structural Properties of Sb_2S_3 under Pressure: Evidence of an Electronic Topological Transition. *Sci. Rep.* **2016**, *6*, 24246.

(41) Ibañez, J.; Sans, J.A.; Popescu, C.; López-Vidrier, J.; Elvira-Betanzos, J. J.; Cuenca-Gotor, V. P.; Gomis, O.; Manjón, F. J.; Rodríguez-Hernández, P.; Muñoz, A. Structural, Vibrational, and Electronic Study of Sb_2S_3 at High Pressure. *J. Phys. Chem. C* **2016**, *120*, 10547.

(42) Zhao, J.G.; Yang, L.X.; Yu, Z.H.; Wang, Y.; Li, C.Y.; Yang, K.; Liu, Z.G.; Wang, Y. Structural Phase Transitions and Metallized Phenomena in Arsenic Telluride under High Pressure. *Inorg. Chem.* **2016**, *55*, 3907.

(43) Zhang, Y.H.; Ma, Y.M.; Geng, A.H.; Zhu, C.Y.; Liu, G.T.; Tao, Q.; Li, F.F.; Wang, Q.L.; Li, Y.; Wang, X. et al. Pressure-Induced Electronic Phase Transitions of α-As_2Te_3. *J. Alloys Comp.* **2016**, *685*, 551-558.

(44) Morin, C.; Corallini, S.; Carreaud, J.; Vaney, J.B.; Delaizir, G.; Crivello, J.C.; Lopes, E.B.; Piarristeguy, A.; Monnier, J.; Candolfi, C. et al. Polymorphism in Thermoelectric As_2Te_3. *Inog. Chem.* **2015**, *54*, 9936-9947.

(45) Pal, K.; Waghmare, U.V. Strain Induced Z_2 Topological Insulating State of β-As_2Te_3. *App. Phys. Lett.* **2014**, *105*, 062105.

(46) Sakai, N.; Fritzsche, H. Semiconductor-Metal and Superconducting Transitions Induced by Pressure in Amorphous As_2Te_3. *Phys. Rev. B* **1977**, *15*, 973-978.

(47) Kristofik, J.; Mares, J.J.; Smid, V. The Effect of Pressure on Conductivity and Permittivity of As_2Te_3-Based Glasses. *Phys. Stat. Sol. (a)* **1985**, *89*, 333-345.

(48) Parthasarathy, G.; Gopal, E.S.R. Effect of High Pressure on Chalcogenide Glasses. *Bull. Mater. Sci.* **1985**, *7*, 271-302.

(49) Hoshino, H.; Miyanaga, T.; Ikemoto, H.; Hosoyawas, S.; Endo, H. The Semiconductor-Metal Transition of Liquid Arsenic-Selenium Mixtures at High Temperatures and High Pressures. *J. Non-Cryst. Sol.* **1996**, *205-207*, 43-47.

(50) Shimojo, F.; Hoshino, K.; Zempo, Y. Atomic and Electronic Structures in Liquid Arsenic Telluride by *ab initio* Molecular Dynamics Simulations. *J. Phys.: Condens. Matter* **2002**, *14*, 8425-8433.

(51) Struzhkin, V.V.; Goncharov, A.F.; Caracas, R.; Mao, H.K.; Hemley, R.J. Synchrotron Infrared Spectroscopy of the Pressure-Induced Insulator-Metal Transitions in Glassy As_2S_3 and As_2Se_3. *Phys. Rev. B* **2008**, *77*, 165133.

(52) Ramesh, K. Pressure Dependence of Glass Transition in As_2Te_3 Glass. *J. Phys.Chem. B* **2014**, *118*, 8848-8853.

(53) Fauth, F.; Peral, I.; Popescu, C.; Knapp, M. The New Material Science Powder Diffraction Beamline at ALBA Synchrotron. *Powder Diffr.* **2013**, *28*, S360−S370.

(54) Hammersley, A. P.; Svensson, S. O.; Hanfland, M.; Fitch, A. N.; Hausermann, D. Two-Dimensional Detector Software: From Real¨ Detector to Idealised Image or Two-Theta Scan. *High Pressure Res.* **1996**, *14*, 235−248.

(55) Larson, A.C.; von Dreele, R.B. General Structure Analysis System (GSAS). *LANL Report* **2004**, *86*, 748.

(56) Toby, B. H. EXPGUI, A Graphical User Interface for GSAS. *J. Appl. Crystallogr.* **2001**, *34*, 210−213.

(57) Momma, K.; Izumi, F. VESTA 3 for -Three-dimensional Visualization of Crystal, Volumetric and Morphology Data. *J. Appl. Crystallogr.* **2011**, *44*, 1272-1276.

(58) Dewaele, A.; Loubeyre, P.; Mezouar, M. Equations of State of Six Metals above 94 GPa. *Phys. Rev. B* **2004**, *70*, 094112.

(59) Mao, M. K.; Xu, J.; Bell, P. M. Calibration of the Ruby Pressure Gauge to 800 kbar under Quasi-Hydrostatic Conditions. *J. Geophys. Res.* **1986**, *91*, 4673−4676.

(60) Piermarini, G.J.; Block, S.; Barnett, J.D. Hydrostatic Limits in Liquids and Solids to 100 kbar. *J. Appl. Phys.* **1973**, *44*, 5377-5382.

(61) Klotz, S.; Chervin, J.-C.; Munsch, P.; Le Marchand, G. Hydrostatic Limits of 11 Pressure Transmitting Media. *J. Phys. D : Appl. Phys.* **2009**, *42*, 075413.

(62) Hohenberg, P.; Kohn, W. Inhomogeneous Electron Gas. *Phys. Rev.* **1964**, *136*, B864-B871.

(63) Kresse, G.; Hafner, J. Ab Initio Molecular Dynamics for Liquid Metals. *Phys. Rev. B* **1993**, *47*, 558−561.

(64) Kresse, G.; Furthmüller, J. Efficiency of ab-initio Total Energy Calculations for Metals and Semiconductors Using a Plane-wave Basis Set. *Comput. Mat. Sci.* **1996**, *6*, 15-50.

(65) Kresse, G.; Furthmüller, J. Efficient Iterative Schemes for ab initio Total-energy Calculations Using a Plane-wave Basis Set. *Phys. Rev. B* **1996**, *54*, 11169-11186.

(66) Blöchl, P. E. Projector Augmented-Wave Method. *Phys. Rev. B* **1994**, *50*, 17953−17979;

(67) Kresse, G.; Joubert, D. From Ultrasoft Pseudopotentials to the Projector Augmented-wave Method. *Phys. Rev. B* **1999**, *59*, 1758-1775.

(68) Perdew, J. P.; Burke, K.; Ernzerhof, M. Generalized Gradient Approximation Made Simple. *Phys. Rev. Lett.* **1996**, *77*, 3865-3868

(69) Parlinski, K.; Li, Z. Q.; Kawazoe, Y. First-Principles Determination of the Soft Mode in Cubic ZrO_2. *Phys. Rev. Lett.* **1997**, *78*, 4063−4066.

(70) Deng, H. Theoretical Prediction of the Structural, Electronic, Mechanical and Thermodynamic Properties of the Binary α-As_2Te_3 and β-As_2Te_3. *J. Alloys and Comp.* **2015**, *656*, 695-701.

(71) Kroumova, E.; Aroyo, M.I.; Perez-Mato, J.M.; Kirov, A.; Capillas, C.; Ivantchev, S.; Wondratschek, H. Bilbao Crystallographic Server: Useful Databases and Tools for Phase-Transition Studies. *Phase Transitions* **2003**, *76*, 155-170.

(72) Mendoza-Galván, A.; García-García, E.; Vorobiev, Y.V.; González-Hernández, J. Structural, Optical and Electrical Characterization of Amorphous Se_xTe_{1-x} Thin Film Alloys. *Microelectron. Eng.* **2000**, *51-52*, 677-687.

(73) Usuki, T.; Saitoh, K.; Endo, M.; Uemura, O. Short-range Order of Amorphous and Liquid As-Te-I System, *J. Non-Cryst. Solids* **1996**, *205-207*, 184-188.

(74) Tverjanovich, A.; Rodionov, K.; Bychkov, E. Raman Spectroscopy of Glasses in the As-Te System. *J. Solid State Chem.* **2012**, *190*, 271-276.

(75) Alekberov, R.I.; Mekhtiyeva, S.I.; Isayeva, G.A.; Isayev, A.I. Raman Scattering in As-Se-S and As-Se-Te Chalcogenide Vitreous Semiconductors, *Semic.* **2014**, *48*, 800-803.

(76) Taylor, P.C.; Bishop, S.G.; Mitchell, D.L. Infrared Properties of AsxTe1-x Glasses, *Solid State Commun.* **1975**, *16*, 167-170.

(77) Lukic, S.R.; Petrovic, D.M.; Skuban, S.J.; Radonjic, Lj.; Cvejic, Z. Formation of Complex Structural Units and Structure of As-S-Se-Te-I Glasses. *J. Opt. Adv. Mat.* **2003**, *5*, 1223-12229.

(78) Zallen, R.; Slade, M.L.; Ward, A.T. Lattice Vibrations and Interlayer Interactions in Crystalline As_2S_3 and As_2Se_3. *Phys. Rev. B* **1971**, *3*, 4257-4273.

(79) Pine, A.S; Dresselhaus, G. Raman Spectra and Lattice Dynamics of Tellurium. *Phys. Rev. B* **1971**, *4*, 356-371.

(80) Canepa P.; Hanson, R. M.; Ugliengo, P.; Alfredsson, M. J-ICE: a New Jmol Interface for Handling and Visualizing Crystallographic and Electronic Properties. *J. Appl. Cryst.* **2011**, *44*, 225-229.

(81) Pereira, A. L. J.; Gomis, O.; Sans, J. A.; Pellicer-Porres, J.; Manjón, F. J.; Beltrán, A.; Rodríguez-Hernández, P.; Muñoz, A. Pressure Effects on the Vibrational Properties of α-Bi_2O_3: an Experimental and Theoretical Study. J. Phys.: Condens. Matter **2014**, *26*, 225401.

(82) Birch, F. The Effect of Pressure Upon the Elastic Parameters of Isotropic Solids, According to Murnaghan's Theory of Finite Strain. *J. Appl. Phys.* **1938**, *9*, 279-288.

(83) Errandonea, D.; Popescu, C.; Achary, S.N.; Tyagi, A.K.; Bettinelli, M. In situ High-Pressure Synchrotron X-ray Diffraction Study of the Structural Stability in NdVO4 and LaVO4. Mat. Res. Bull. **2014**, *50*, 279-284.

(84) Sans, J.A.; Manjón, F.J.; Pereira, A.L.J.; Vilaplana, R.; Gomis, O.; Segura, A.; Muñoz, A.; Rodríguez-Hernández, P.; Popescu, C.; Drasar, C. et al. Structural, Vibrational, and Electrical Study of Compressed BiTeBr. *Phys. Rev. B* **2016**, *93*, 024110.

(85) Haussühl, S. Physical Properties of Crystals. An Introduction, Wiley-VCH, Weinheim, 2007.

(86) Angel, R. J. http://www.rossangel.com/text_strain.htm

(87) Vilaplana, R.; Santamaría-Pérez, D.; Gomis, O.; Manjón, F.J.; González, J.; Segura, A.; Muñoz, A.; Rodríguez-Hernández, P.; Pérez-González, E.; Marín-Borrás, V. et al. Structural and Vibrational Study of Bi_2Se_3 under High Pressure. *Phys. Rev. B* **2011**, *84*, 184110.

(88) Pereira, A.L.J.; Sans, J. A.; Gomis, O.; Manjon, F.J.; Rodríguez-Hernández, P.; Muñoz, A.; Popescu, C.; Beltrán, A. lsostructural Second-Order Phase Transition of β-Bi_2O_3 at High Pressures: An Experimental and Theoretical Study. *J. Phys. Chem. C* **2014**, *118*, 23189-23201.

(89) Walsh, A.; Payne, D.J.; Egdell, R.G.; Watson, G.W. Stereochemistry of Post-Transition Metal Oxides: Revision of the Classical Lone Pair Model. *Chem. Soc. Rev.* **2011**, *40*, 4455-4463.

(90) Lundegaard, L.F.; Miletich, R.; Balic-Zunic, T.; Makovicky, E. Equation of State and Crystal Structure of Sb_2S_3 between 0 and 10 GPa. *Phys. Chem. Minerals* **2003**, *30*, 463-468.

(91) Lundegaard, L.F.; Makovicky, E.E.; Boffa-Ballaran, T.; Balic-Zunic, T. Crystal Structure and Cation Lone Electron Pair Activity of Bi_2S_3 between 0 and 10 GPa. *Phys. Chem. Minerals* **2005**, *32*, 578-584.

(92) Pereira, A.L.J.; Gracia, L.; Santamaría-Pérez, D.; Vilaplana, R.; Manjón, F.J.; Errandonea, D; Nalin, M.; Beltrán, A. Structural and Vibrational Study of Cubic Sb_2O_3 at under High Pressure. *Phys. Rev. B* **2012**, *85*, 174108.

(93) Zhao, K.; Wang, Y.; Xin, C. Wang, X.J,; Wang, Y.; Liu, Z.G.; Li, B.S. First Principles Study of Isostructural Phase Transition in Sb2Te3 under High Pressure. *Phys. Stat. Sol. RRL* **2015**, *9*, 379-383.

(94) Richter, W.; Renucci, J.B.; Cardona, M. Hydrostatic Pressure Dependence of First-Order Raman Frequencies in Se and Te. *Phys. Stat. Sol. (b)* **1973**, *56*, 223-229.

(95) Aoki, K.; Shimomura, O.; Minomura, S.; Koshizuka, N.; Tsushima, T. Raman Scattering of Trigonal Se and Te at Very High Pressure. *J. Phys. Soc. Jpn.* **1980**, *48*, 906-911.

(96) Rodríguez-Fernández, C.; Manzano, C. V.; Romero, A. H.; Martín, J.; Martín-González, M.; Morais de Lima Jr, M.; Cantarero. A. The Fingerprint of Te-rich and Stoichiometric Bi_2Te_3 Nanowires by Raman Spectroscopy. *Nanotechnology* **2016**, *27*, 075706.

(97) Lindberg, G. P.; Tallman, R. E.; Lauck, R.; Cardona, M.; Liu, X.; Furdyna, J. K.; Weinstein, B. A. Effects of Pressure on Photo-Induced Formation of Se and Te Clusters in II–VI Compounds. *Phys. Status Solidi B* **2013**, *250*, 711− 715.

(98) Vilaplana, R.; Gomis, O.; Manjón, F. J.; Ortiz, H. M.; Pérez-González, E.; López-Solano, J.; Rodríguez-Hernández, P.; Muñoz, A.; Errandonea, D.; Ursaki, V. V. et al. Lattice Dynamics Study of $HgGa_2Se_4$ at High Pressures. *J. Phys. Chem. C* **2013**, *117*, 15773-15781.

(99) Popescu, M.A. Non-crystalline chalcogenides. Dordrecht, Kluwer Academic Publishing (2000).

(100) Fayek, S.A.; Balboul, M.R.; Marzouk, K.H. Optical, Electrical and Thermal Studies on $(As_2Se_3)_{3−x}(As_2Te_3)_x$ Glasses. *Thin Solid Films* **2007**, *515*, 7281-7285.

TABLES.

Atoms	Site	Character	x	y	z
As1	*4i*	Exp	0.6117(4)	0	0.4436(9)
		The	0.6218		0.4408
As2	*4i*	Exp	0.7917(7)	0	0.8608(13)
		The	0.7962		0.8593
Te1	*4i*	Exp	0.972(3)	0	0.7143(6)
		The	0.9619		0.7137
Te2	*4i*	Exp	0.778(3)	0	0.3391(7)
		The	0.7812		0.3371
Te3	*4i*	Exp	0.623(3)	0	0.9682(6)
		The	0.6284		0.9664

Table 1. Experimental and theoretical fractional coordinates corresponding to the *C2/m* phase of α-As_2Te_3 at ambient conditions. Experimental (exp) lattice parameters and volume are: $a =$ 14.3441(4) Å, $b =$ 4.01627(19) Å, $c =$ 9.8895(4) Å, $\beta =$ 95.053(3)º and $V_0 =$ 567.52(3) Å^3. Theoretical (the) lattice parameters and volume are: $a =$ 14.7995 Å, $b =$ 4.0744 Å, $c =$ 10.0667 Å, $\beta =$ 95.8181º and $V_0 =$ 603.88 Å^3.

Mode	*Ab initio* calculations			Experiment		
	$\omega_0\ (cm^{-1})$	$\alpha\left(\frac{cm^{-1}}{GPa}\right)$	$\beta\left(\frac{cm^{-1}}{GPa^2}\right)$	$\omega_0\ (cm^{-1})$	$\alpha\left(\frac{cm^{-1}}{GPa}\right)$	$\beta\left(\frac{cm^{-1}}{GPa^2}\right)$
Ag^1	43.0(6)	1.2(5)	-0.10(4)	49.0(2)	2.5(5)	-0.19(5)
Ag^2	47.4(5)	3.4(3)	-0.070(17)	67.0(4)	4.3(2)	-0.15(3)
Bg^1	48.3(7)	1.5(2)	-0.077(19)	66.0(4)	0.15(6)	-0.014(4)
Bg^2	62.4(2)	2.0(1)	-0.011(5)			
Ag^3	63.8(1)	3.8(2)	-0.08(1)			
Ag^4	83.0(5)	2.9(1)	-0.08(1)	90.6(3)	1.8(1)	-0.037(9)
Bg^3	95.6(3)	4.5(3)	-0.15(2)	99.0(8)	6.0(8)	-0.7(2)
Ag^5	99.1(4)	2.6(1)	-0.068(9)			
Bg^4	107.9(2)	3.2(2)	-0.04(1)	119.2(2)	2.2(1)	-0.045(9)
A_1(Te)				123.1(4)	-3.4(3)	0.13(5)
Ag^6	117.7(2)	1.9(3)	-0.005(2)			
Ag^7	121.0(3)	2.8(3)	-0.018(3)	128.0(8)	2.3(4)	-0.02(3)
Bg^5	130.9(4)	1.5(1)	0.05(1)	137.0(9)	-0.8(4)	0.16(2)
E''(Te)				142.0(3)	-0.6(2)	0.11(4)
Ag^8	170.2(4)	-1.3(2)	0.17(2)	171.4(3)	-0.3(1)	0.13(3)
Ag^9	177.3(2)	0.22(6)	0.074(5)			
Ag^{10}	192.0(1)	-1.3 (3)	0.14(2)	193.2(3)	0.13(5)	0.066(8)

Table 2. Theoretical and experimental Raman mode frequencies and their pressure coefficients in α-As$_2$Te$_3$ at room temperature as fitted with equation $\omega(P) = \omega_0 + \alpha P + \beta P^2$.

(a)

(b)

(c)
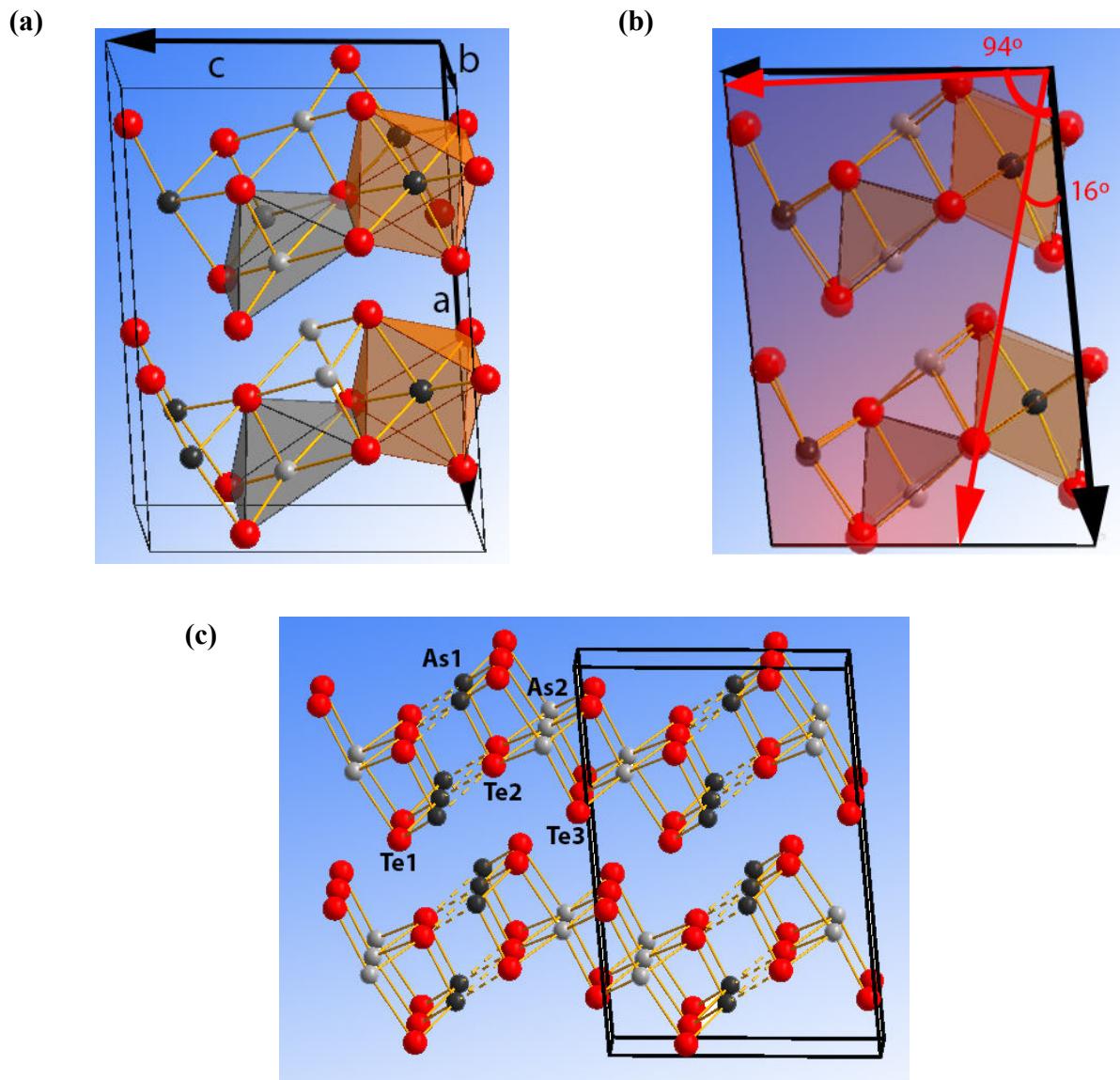
Figure 1. (a) Scheme of α-As$_2$Te$_3$ structure at room pressure. **(b)** Representation of the effect of pressure in the α-As$_2$Te$_3$ structure at 1 atm (base scheme) and 14 GPa (scaled and superimposed, transparent scheme). Atoms at 14 GPa seem greater than at 1atm due to rescaling of cell axes to match the values at 1 atm. Dark grey, light grey and red colors correspond to As1, As2 and Te atoms, respectively. Red arrow indicates the direction of maximum compressibility of the compound at room and high pressure. **(c)** Layer and rod layout.
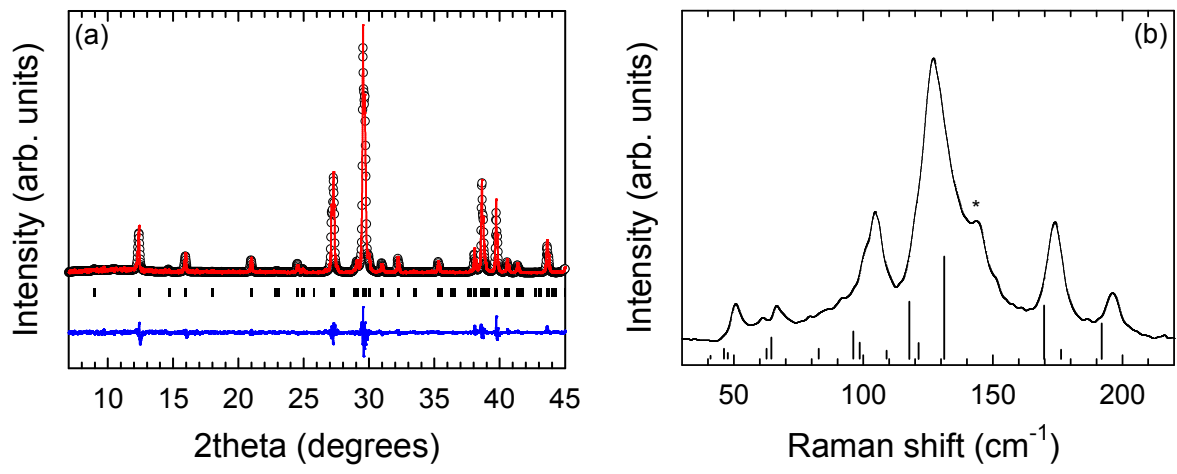
Figure 2. Structural and vibrational characterization of α-As$_2$Te$_3$ at room conditions: **(a)** Powder XRD pattern. Rietveld refinement and residuals are also plotted. **(b)** RS spectrum. Bottom marks show theoretical Raman-active mode frequencies whose length scales with the calculated intensity for each mode. The asterisk indicates a peak from crystalline Te.
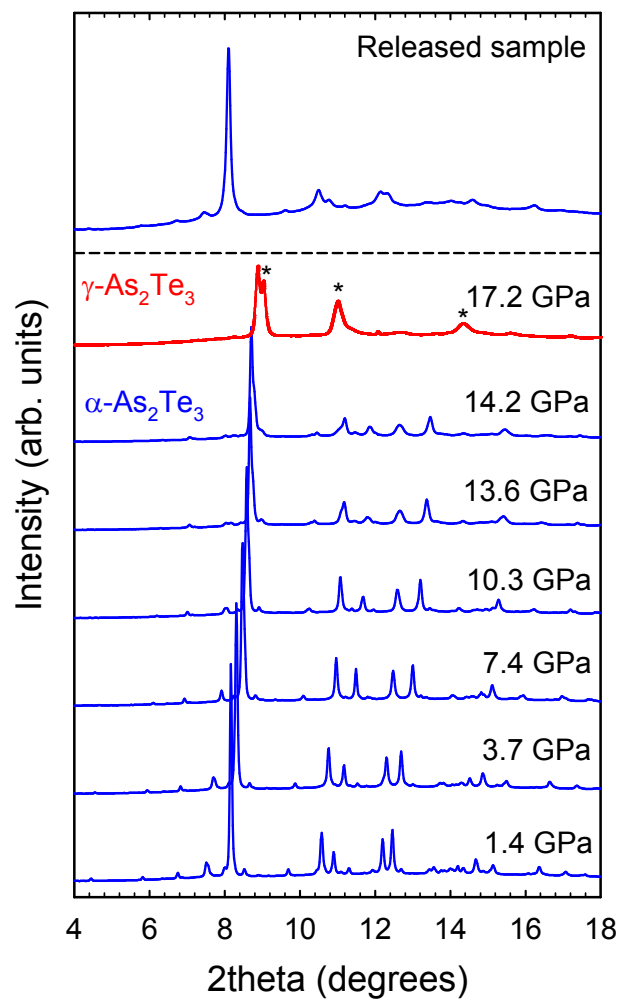
Figure 3. Powder HP-XRD patterns of α-As$_2$Te$_3$ at selected pressures up to 17.2 GPa where the sample transits to a γ-As$_2$Te$_3$. Patterns are shifted in vertical for comparison.
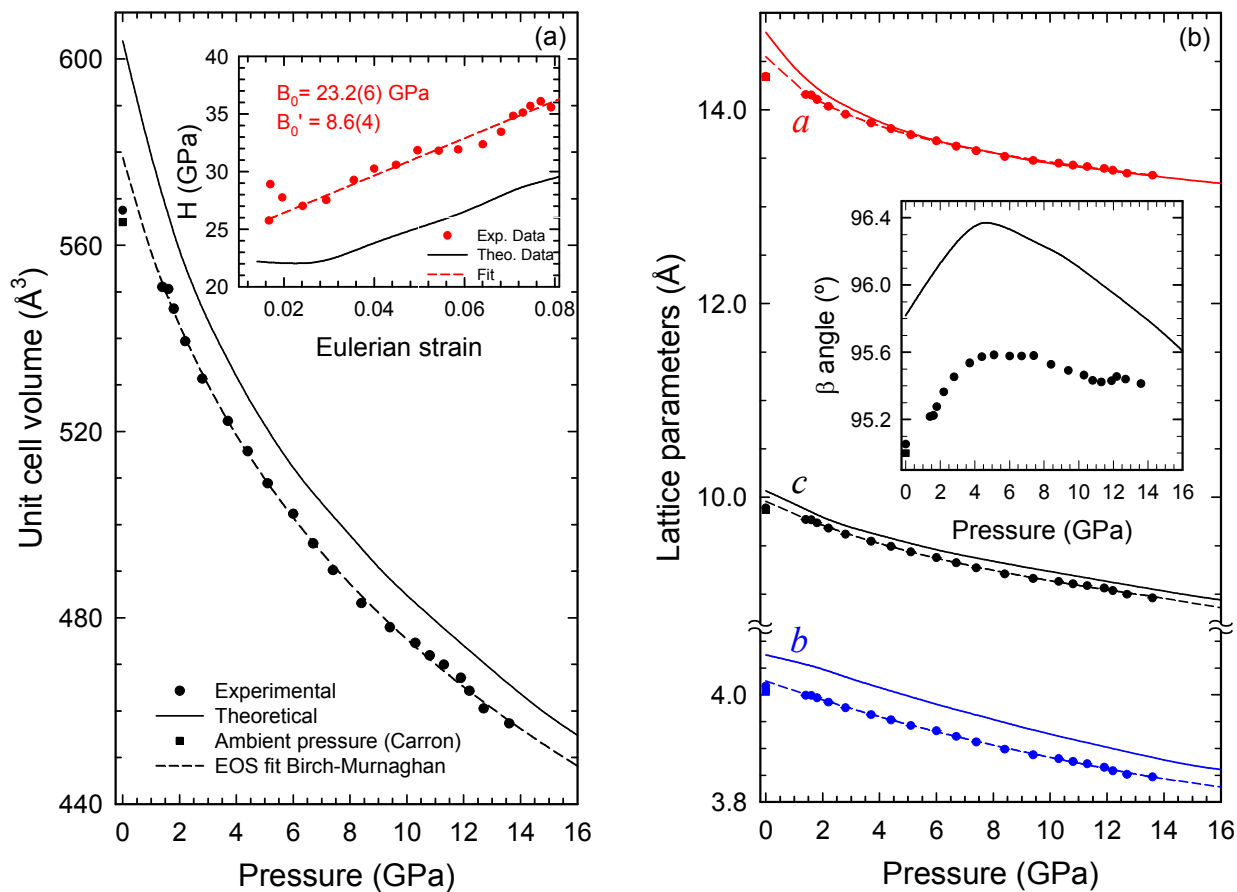
Figure 4. Experimental (symbols) and theoretical (solid lines) pressure dependence of the unit-cell volume **(a)** and lattice parameters **(b)** in α-As_2Te_3. Experimental data are fit to a BM-EoS (dashed lines) and compared to theoretical data. Inset of Fig. 4a shows the normalized pressure vs Eulerian strain plot for both experimental and theoretical data. Inset of Fig. 4b shows the pressure dependence of the monoclinic β angle. Squares correspond to data at ambient pressure taken from Ref. 32.
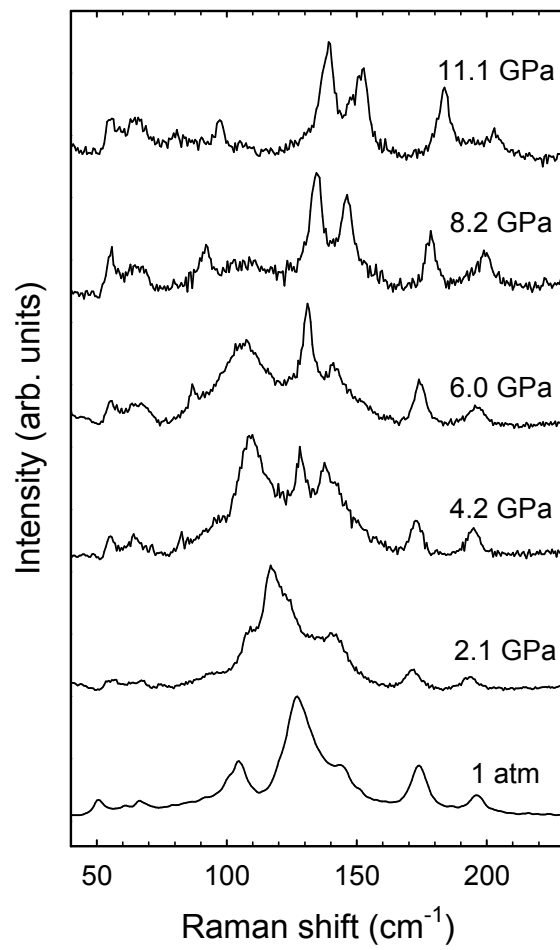
Figure 5. Room-temperature Raman scattering spectra of α-As₂Te₃ at selected pressures.
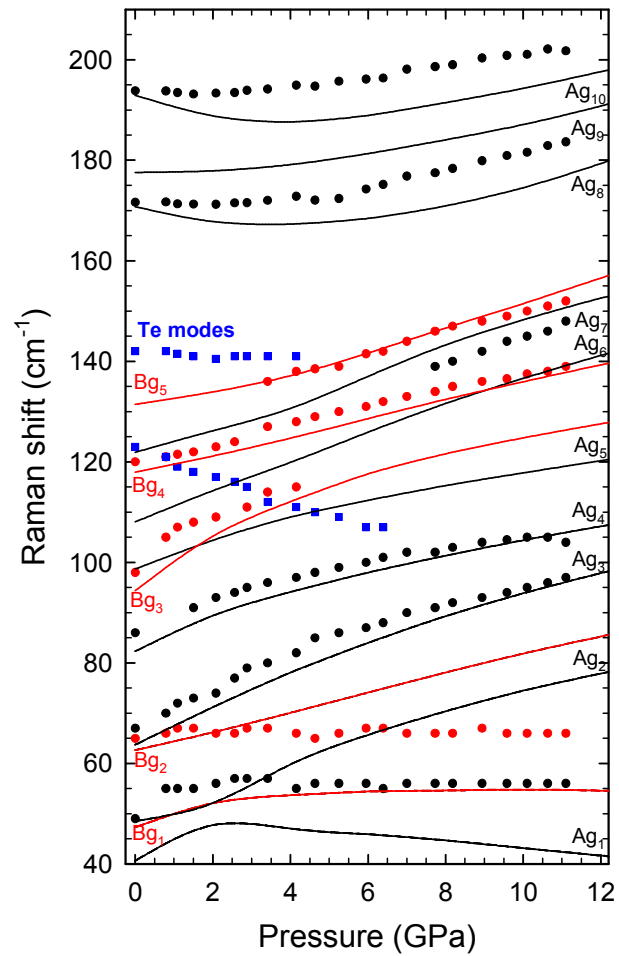
Figure 6. Experimental (symbols) and theoretical (lines) pressure dependence of the Raman-mode frequencies of α-As₂Te₃. Different colors represent Raman-active modes of different symmetries. Blue squares represent the modes corresponding to crystalline Te.
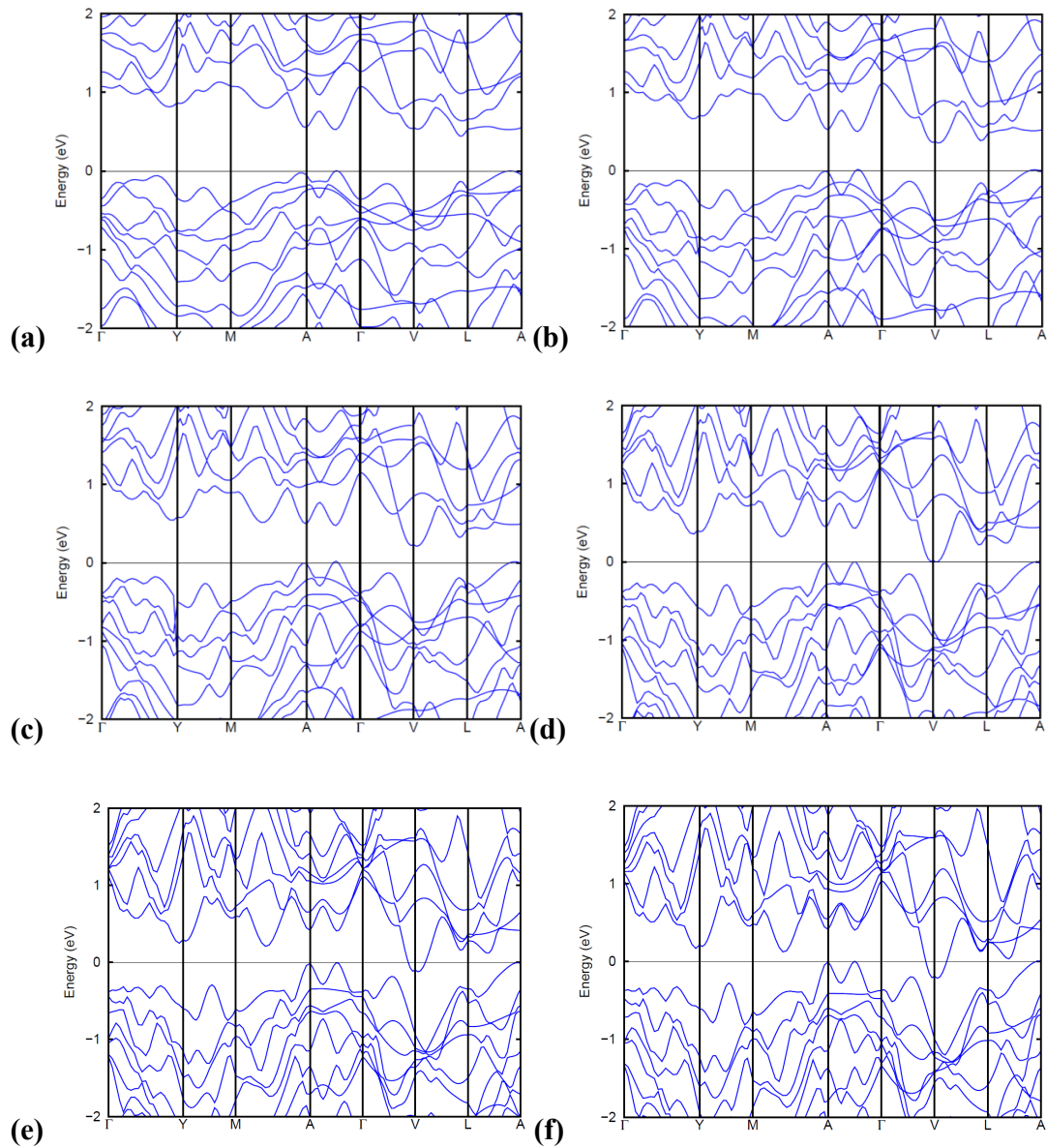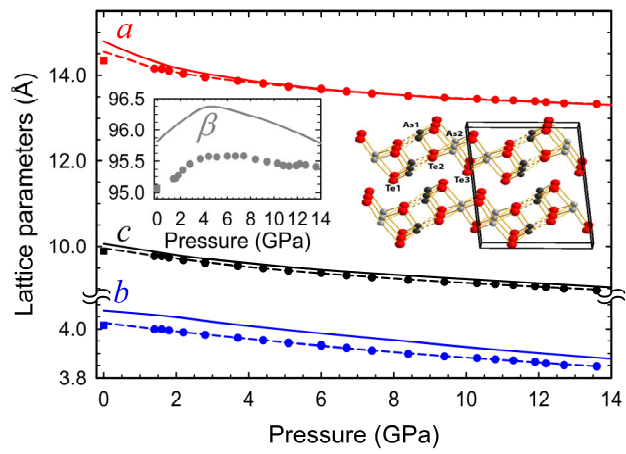
Figure 7. Calculated band structure of α-As$_2$Te$_3$ at different pressures: **(a)** 0 GPa, **(b)** 1 GPa, **(c)** 2 GPa, **(d)** 4 GPa, **(e)** 6 GPa, and **(f)** 8 GPa.

Table of Contents Graphic and Synopsis

Structural, Vibrational and Electronic Study of α-As2Te3 under Compression

V.P. Cuenca-Gotor,[1] J.A. Sans,[1,] J. Ibáñez,[2] C. Popescu,[3] O.Gomis,[4] R. Vilaplana,[4] F.J. Manjón,[1] A. Leonardo,[5,6] E. Sagasta,[7] A. Suárez-Alcubilla,[8,9] I.G. Gurtubay,[6,8] M. Mollar,[1] and A. Bergara[6,8,9]*

1 Instituto de Diseño para la Fabricación y Producción Automatizada, Universitat Politècnica de València, 46022 Valencia (Spain)

2 Institut de Ciències de la Terra Jaume Almera, CSIC, Barcelona (Spain)

3 ALBA-CELLS, 08290 Cerdanyola, Barcelona (Spain)

4 Centro de Tecnologías Físicas, Universitat Politècnica de València, 46022 Valencia (Spain)

5 Dpto. de Física Aplicada II, Universidad del País Vasco, UPV/EHU, 48080 Bilbao (Spain)

6 Donostia International Physics Center (DIPC), 20018 Donostia (Spain)

7 CIC NanoGUNE, E-20018, Donostia, San Sebastián (Spain)

8 Dpto. de Física de la Materia Condensada, Universidad del País Vasco, UPV/EHU, 48080 Bilbao (Spain)

9 Centro de Física de Materiales CFM, Centro Mixto CSIC-UPV/EHU, 20018 Donostia (Spain)

*Corresponding author: J.A. Sans (juasant2@upv.es)

Lattice dynamics of α-As$_2$Te$_3$ at room pressure

The RS spectrum of α-As$_2$Te$_3$ at room pressure has a close similarity to RS spectra reported in glasses containing As and Te atoms which show vibrational frequencies below 200 cm^{-1}. Modes between 150 and 160 cm^{-1} were attributed to Te-Te vibrations as in amorphous Te in Refs. [1-4]. Modes between 175 and 195 cm^{-1} have been attributed to As-Te vibrations [2-6]. Finally, modes between 230 and 240 cm^{-1} have been attributed to amorphous As [3,5]. The mode whose frequency is around 195 cm^{-1} is in good agreement with RS measurement in As$_2$Se$_3$, whose highest vibrational modes is around 250 cm^{-1} [7] as already commented by Tverjanovich et al. [3]. These two modes scale perfectly with the square root masses of Se and Te, thus giving support to the assignment of the mode around 195 cm^{-1} to the stretching vibrations of As-Te.

Visualization of the vibrational modes of α-As$_2$Te$_3$ at Γ calculated from *first principles* using the VASP code can be performed with the J-ICE software [8]. This visualization has allowed us to further understand the complex lattice dynamics of this compound as it was previously done for monoclinic α-Bi$_2$O$_3$ [9]. In general, we have observed that the motion of atoms is very complex and no modes related to isolated molecular units can be identified in monoclinic As$_2$Te$_3$. Modes with frequencies above 160 cm^{-1} are dominated by the vibration of light As atoms; modes with frequencies between 100 and 150 cm^{-1} are mainly determined by the vibration of heavy Te atoms; and modes with frequencies below 100 cm^{-1} are collective or lattice modes of vibration where groups of As and Te atoms move in or out of phase. As matter of example **Fig. S1** shows the atomic vibrations in four Raman-active vibrational modes. The highest vibrational Raman mode Ag^{10} mode shows the strong movement of As atoms in the a-c plane (**Fig. S1a**); the Ag^7 mode (**Fig. S1b**) corresponds to an almost pure vibration of Te atoms; the lowest Bg^1 mode (**Fig. S1c**) corresponds to a half shear mode between alternated layers with atoms vibrating along the *b* axis (note that the structure is shifted in this view to see the atom movements along the *b* axis perpendicular to *a* and *c* axis); and the Ag^1 mode (**Fig. S1d**) is the lowest-frequency Raman mode. In this complex monoclinic layered structure, there is no pure shear mode of the layers either in the *a-c* plane or along the *b* axis (either Raman or IR-active).
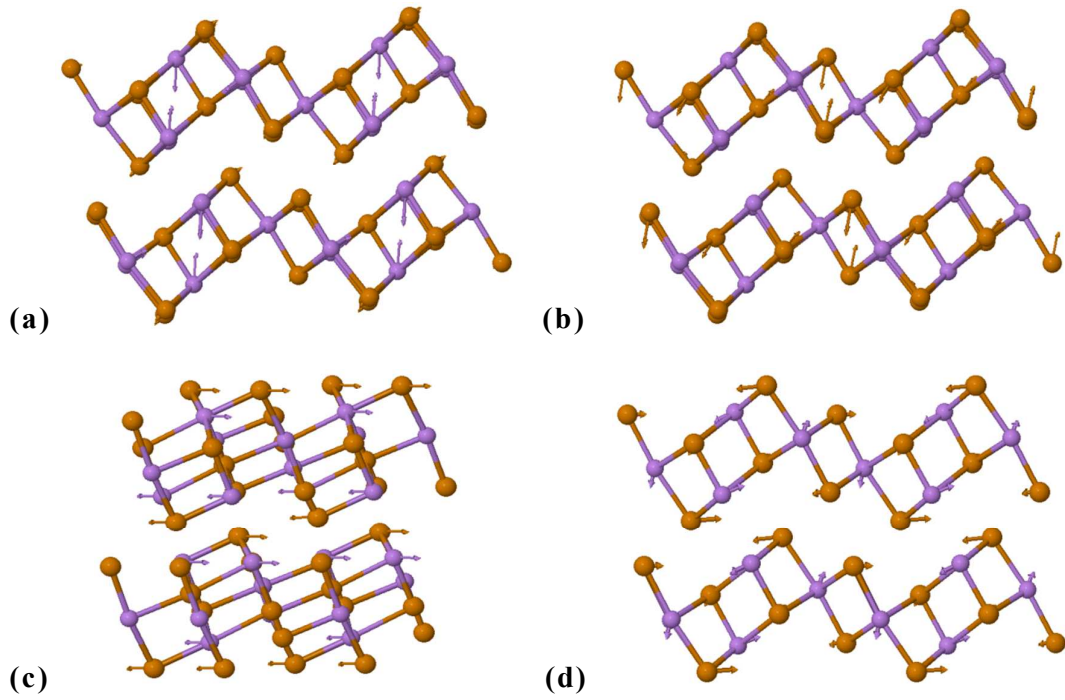
Figure S1. Scheme of atomic vibrations (As atoms are violet circles and Te atoms are orange circles) in some Raman-active vibrational modes of α-As$_2$Te$_3$: (a) Ag^{10} mode (optical mode of highest frequency), (b) Ag^7 mode (pure vibration of Te atoms), (c) Bg^1 mode (half shear mode along b axis), and (d) Ag^1 mode (optical mode of lowest frequency which is not a pure shear mode in the a-c plane).

Rietveld and LeBail analysis of HP-XRD measurements of α-As$_2$Te$_3$ under pressure
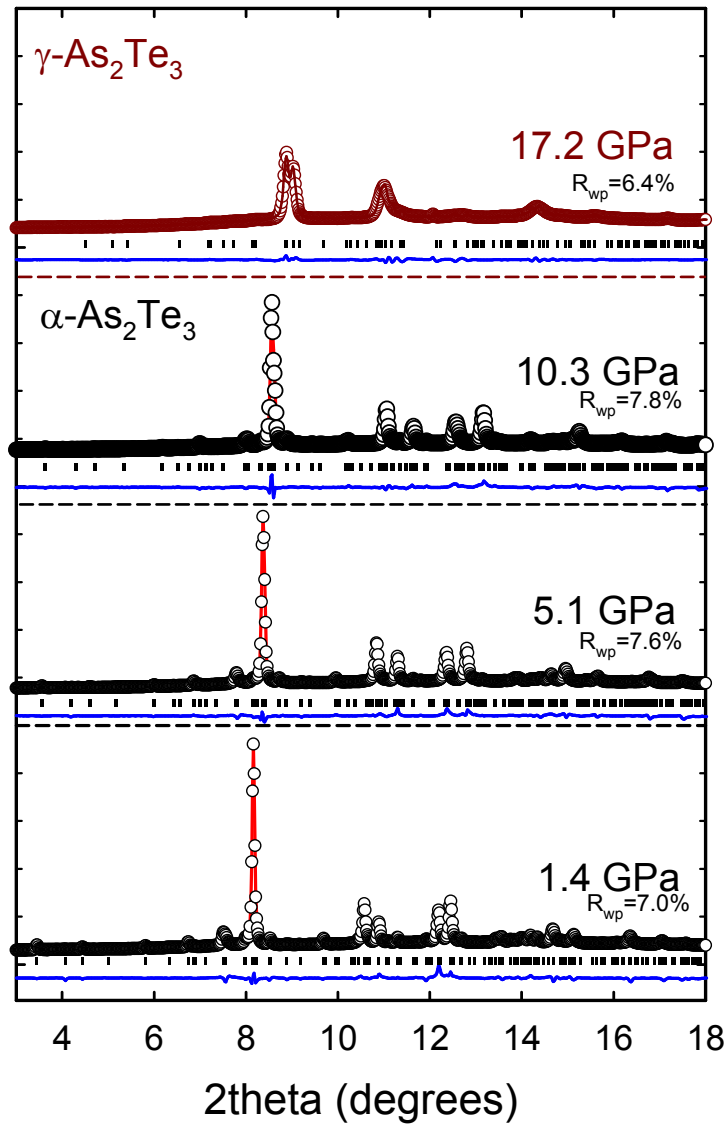
Figure S2. Rietveld refinement at two different pressures (1.4 and 5.1 GPa) and Le Bail refinement (10.3 GPa) for α-As$_2$Te$_3$. Le Bail analysis for γ-As$_2$Te$_3$ is also reported at 20 GPa. Experimental diffraction patterns are plotted as symbols, with the refined pattern as red lines and the residuals as blue lines. Vertical ticks represent theoretical position of the Bragg reflections both in α-As$_2$Te$_3$ and γ-As$_2$Te$_3$.
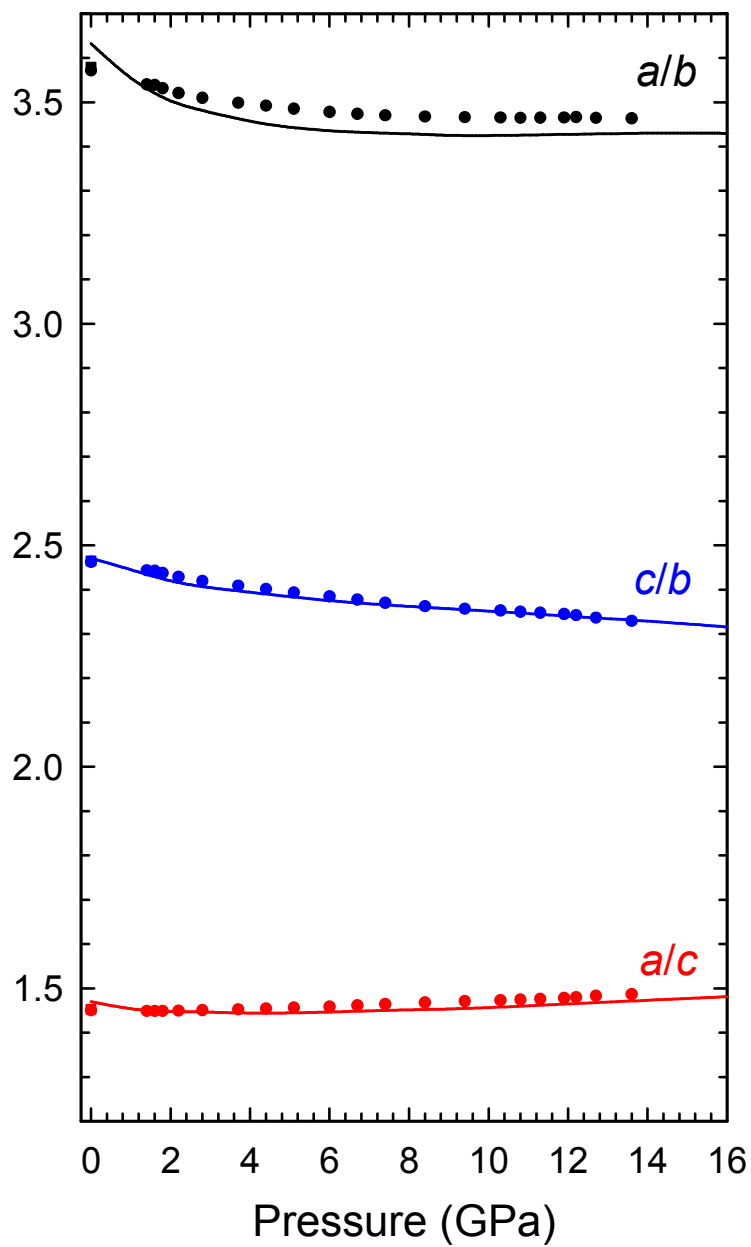
Figure S3. Experimental (symbols) and theoretical (solid lines) pressure dependence of the axial ratios of α-As$_2$Te$_3$ under compression. Squares correspond to data at ambient pressure taken from Ref. 10.

Calculation of the experimental and theoretical compressibility tensor at different pressures

The isothermal compressibility tensor, β_{ij}, is a symmetric second rank tensor that relates the state of strain of a crystal to the change in pressure that induced it [11]. The tensor coefficients for a monoclinic crystal with b as the unique crystallographic axis are:

$$\beta_{ij} = \begin{pmatrix} \beta_{11} & 0 & \beta_{13} \\ 0 & \beta_{22} & 0 \\ \beta_{13} & 0 & \beta_{33} \end{pmatrix}$$

We have obtained the isothermal compressibility tensor coefficients for α-As$_2$Te$_3$ at several pressures using the IRE (Institute of Radio Engineers) convention for the orthonormal basis for the tensor: $e_3\|c$, $e_2\|b^*$, $e_1\|e_2\times e_3$. The tensor has been obtained with the finite Eulerian approximation as implemented in the Win_Strain package [12].

The change of the β monoclinic angle (always perpendicular to the b axis) with pressure implies that, in this monoclinic compound, the direction of the a axis changes with pressure assuming both b and c axis constant. Furthermore, the departure of this monoclinic angle from 90º indicates that the direction of maximum compressibility is not exactly that of the a axis. Therefore, in order to evaluate the direction of maximum compressibility as a function of pressure we have calculated and diagonalised the experimental and theoretical isothermal compressibility tensor, β_{ij}, at different pressures.

The experimental and theoretical elements of this tensor at different pressures are reported in Tables S1 and S2, respectively, where the directions of the maximum, intermediate and minimum compressibility and the values of the compressibility along those directions are given by the eigenvectors (ev_i, i=1-3) and eigenvalues (λ_i, i=1-3), respectively.

First of all, we have to note that there is a reasonable good agreement between the experimental and calculated axial compressibilities (β_{ii} coefficients) at room pressure because $\beta_{11} > \beta_{33} > \beta_{22}$ in both cases. A diagonalization of the β_{ij} tensor at room pressure yields for our experiments the maximum, intermediate and minimum compressibilities $27.3(2.1)\cdot10^{-3}$, $14.0(1.1)\cdot10^{-3}$ and $4.7(4)\cdot10^{-3}$ GPa^{-1}, respectively; whereas for the case of our calculations the obtained values for the compressibilities are

38(3)· 10^{-3}, 14.6 (1.1)·10^{-3} and 4.3(5)·10^{-3} GPa^{-1}. These experimental (theoretical) results indicate that around 59% (67%) of the total compression at room pressure is being accommodated along the direction of maximum compressibility. Taking into account the eigenvector ev_1, the major compression direction at zero pressure occurs in the (0 1 0) plane at the given angle Ψ (see **Tables S1 and S2**) relative to the *c*-axis (from *c* to *a*) or equivalently at an angle θ relative to the *a*-axis (from *a* to *c*). In particular, the experimental major compression direction at room pressure is at $\theta = 16.0(1.4)°$ from the *a*-axis whereas for our calculations is at 5.5(7)° from the *a*-axis. The direction of intermediate compressibility at room pressure given by eigenvector ev_2 is in the (0 1 0) plane perpendicular to the direction of maximum compressibility, and the direction of minimum compressibility at room pressure given by eigenvector ev_3 is along the *b* axis.

As regards the behaviour of the compressibility tensor under pressure, the most notable feature is that below 2.0 GPa the experimental compressibility of the *a*-axis is higher than that of the *c*-axis ($\beta_{11} > \beta_{33}$); however, at 2.0 GPa both compresibilities are similar, and beyond 3.0 GPa $\beta_{11} < \beta_{33}$ within experimental uncertainties. This behaviour is because the *c*-axis becomes more compressible than the *a*-axis above 3.0 GPa. Furthermore, the decrease of the compressibility of the *a* axis with increasing pressure is so large that the compressibilities of the *a* and *b* axes become equal around 13 GPa ($\beta_{11} = \beta_{22}$). Correspondingly, the direction of maximum compressibility move away the *a*-axis and approaches the *c*-axis with increasing pressure; i.e., the θ angle increases. At 3.0 GPa the direction of maximum compressibility is closer to the *c*-axis than to the *a*-axis and at pressures beyond 5 GPa the direction of maximum compressibility is already very close to the *c*-axis. Note that the results for the evolution of the theoretical tensor under pressure are similar to those obtained for the experimental tensor.

Table S1. Experimental isothermal compressibility tensor coefficients, β_{ij}, and their eigenvalues, λ_i, and eigenvectors, ev_i, for α-As$_2$Te$_3$ at several pressures. The results are given using the finite Eulerian method. The eigenvalues are given in decreasing value along a column.

P(GPa)	0.0	1.0	2.0	3.0	5.0	7.0	9.0	11.0	13.0
β_{11} (10^{-3} GPa^{-1})	26.8 (2.0)	16.5 (1.2)	11.5 (8)	8.7 (6)	5.8 (5)	4.4 (4)	3.5 (3)	2.9 (3)	2.5 (3)
β_{22} (10^{-3} GPa^{-1})	4.7 (5)	4.4 (4)	4.2 (3)	3.9 (3)	3.5 (3)	3.2 (3)	2.9 (3)	2.7 (3)	2.5 (4)
β_{33} (10^{-3} GPa^{-1})	14.5 (1.1)	12.5 (9)	11.0 (8)	9.8 (7)	8.0 (6)	6.8 (5)	5.9 (4)	5.2 (4)	4.6 (4)
β_{13} (10^{-3} GPa^{-1})	2.54 (22)	2.08 (18)	1.56 (15)	1.05 (12)	0.28 (9)	-0.11 (9)	-0.18 (9)	-0.07 (9)	0.04 (9)
λ_1 (10^{-3} GPa^{-1})	27.3 (2.1)	17.4 (1.3)	12.9 (9)	10.4 (8)	8.0 (6)	6.8 (5)	5.9 (4)	5.2 (4)	4.6 (4)
ev_1 (λ_1)	(0.98,0,0.19)	(0.92,0,0.39)	(0.76,0,0.65)	(0.52,0,0.85)	(0.12,0,0.99)	(0.07,0,1.00)	(0.05,0,1.00)	(0.03,0,1.00)	(0.02,0,1.00)
λ_2 (λ_2)	14.0 (1.1)	11.6 (9)	9.7 (7)	8.1 (6)	5.8 (5)	4.4 (4)	3.4 (3)	2.9 (3)	2.5 (3)
ev_2 (λ_2)	(-0.19, 0, 0.98)	(-0.39,0,0.92)	(-0.65,0,0.76)	(-0.85,0,0.52)	(-0.99,0,0.12)	(-1.00,0,0.07)	(-1.00,0,0.05)	(-1.00,0,0.03)	(-1.00,0,0.02)
λ_3 (10^{-3} GPa^{-1})	4.7 (4)	4.4 (4)	4.2 (3)	3.9 (3)	3.5 (3)	3.2 (3)	2.9 (3)	2.7 (3)	2.5 (3)
ev_3 (λ_3)	(0, 1, 0)	(0, 1, 0)	(0, 1, 0)	(0, 1, 0)	(0, 1, 0)	(0, 1, 0)	(0, 1, 0)	(0, 1, 0)	(0, 1, 0)
Ψ, θ (°)[a]	78.8 (1.4), 16.0 (1.4)	66.9 (1.2), 28.2 (1.2)	49.6 (2.3), 45.7 (2.3)	31.4 (2.9), 63.9 (2.9)	7.1 (2.4), 88.5 (2.4)	-2.6 (2.3), 98.2 (2.3)	-4.2 (2.3), 99.7 (2.3)	-1.6 (2.4), 97.0 (2.4)	1.1 (2.4), 94.3 (2.4)

[a] The major compression direction occurs in the (0 1 0) plane at the given angles Ψ to the c-axis (from c to a) and θ to the a-axis (from a to c).

Table S2. Theoretical isothermal compressibility tensor coefficients, β_{ij}, and their eigenvalues, λ_i, and eigenvectors, ev_i, for α-As$_2$Te$_3$ at several pressures. The results are given using the finite Eulerian method. The eigenvalues are given in decreasing value along a column.

P(GPa)	0.0	1.0	3.0	4.0	5.0	7.0	9.0	11.0	13.0
β_{11} (10^{-3} GPa^{-1})	38 (3)	21.4 (1.6)	10.4 (7)	8.2 (6)	6.7 (5)	4.9 (4)	3.9 (3)	3.2 (3)	2.7 (2)
β_{22} (10^{-3} GPa^{-1})	4.3 (5)	4.2 (4)	3.9 (3)	3.8 (3)	3.7 (3)	3.5 (3)	3.3 (3)	3.2 (4)	3.0 (4)
β_{33} (10^{-3} GPa^{-1})	14.6 (1.1)	12.7 (9)	10.0 (7)	9.0 (6)	8.2 (6)	6.9 (5)	6.0 (4)	5.3 (4)	4.8 (4)
β_{13} (10^{-3} GPa^{-1})	-0.14 (2)	0.93 (9)	0.95 (9)	0.53 (7)	-0.005 (9)	-0.34 (7)	-0.43 (7)	-0.54 (7)	-0.63 (8)
λ_1 (10^{-3} GPa^{-1})	38(3)	21.5 (1.6)	11.2 (8)	9.2 (7)	8.2 (6)	7.0 (5)	6.1 (4)	5.4 (4)	4.9 (4)
ev_1 (λ_1)	(1.00,0,0.01)	(0.99,0,0.11)	(0.79,0,0.62)	(0.46,0,0.89)	(0.00,0,1.00)	(0.16,0,-0.99)	(0.19,0,-0.98)	(0.23,0,-0.97)	(0.27,0,-0.96)
λ_2 (10^{-3} GPa^{-1})	14.6 (1.1)	12.6 (9)	9.2 (7)	7.9 (6)	6.7 (5)	4.9 (4)	3.8 (3)	3.2 (7)	3.0 (4)
ev_2 (λ_2)	(0.01,0,1.00)	(0.11,0,-0.99)	(0.62,0,-0.79)	(0.89,0,-0.46)	(1.00,0,0.00)	(0.99,0,0.16)	(0.99,0,0.16)	(0.98,0,0.19)	(0.96,0,0.27)
λ_3 (10^{-3} GPa^{-1})	4.3 (5)	4.2 (4)	3.9 (3)	3.8 (3)	3.7 (3)	3.5 (3)	3.3 (3)	3.1 (5)	2.5 (2)
ev_3 (λ_3)	(0,1,0)	(0,1,0)	(0,1,0)	(0,1,0)	(0,1,0)	(0,1,0)	(0,1,0)	(0,1,0)	(0,1,0)
Ψ, θ (°)[a]	90.3 (7), 5.5 (7)	84.0 (5), 12.0 (5)	51.9 (1.9), 44.4 (1.9)	27.1 (2.8), 69.3 (2.8)	-0.2 (1.6), 96.6 (2.5)	-9.4 (1.7), 105.7 (1.7)	-11.1 (1.6), 107.3 (1.6)	-13.6 (1.7), 109.6 (1.7)	-15.9 (1.8), 111.8 (1.8)

[a] The major compression direction occurs in the (0 1 0) plane at the given angles Ψ to the c-axis (from c to a) and θ to the a-axis (from a to c).
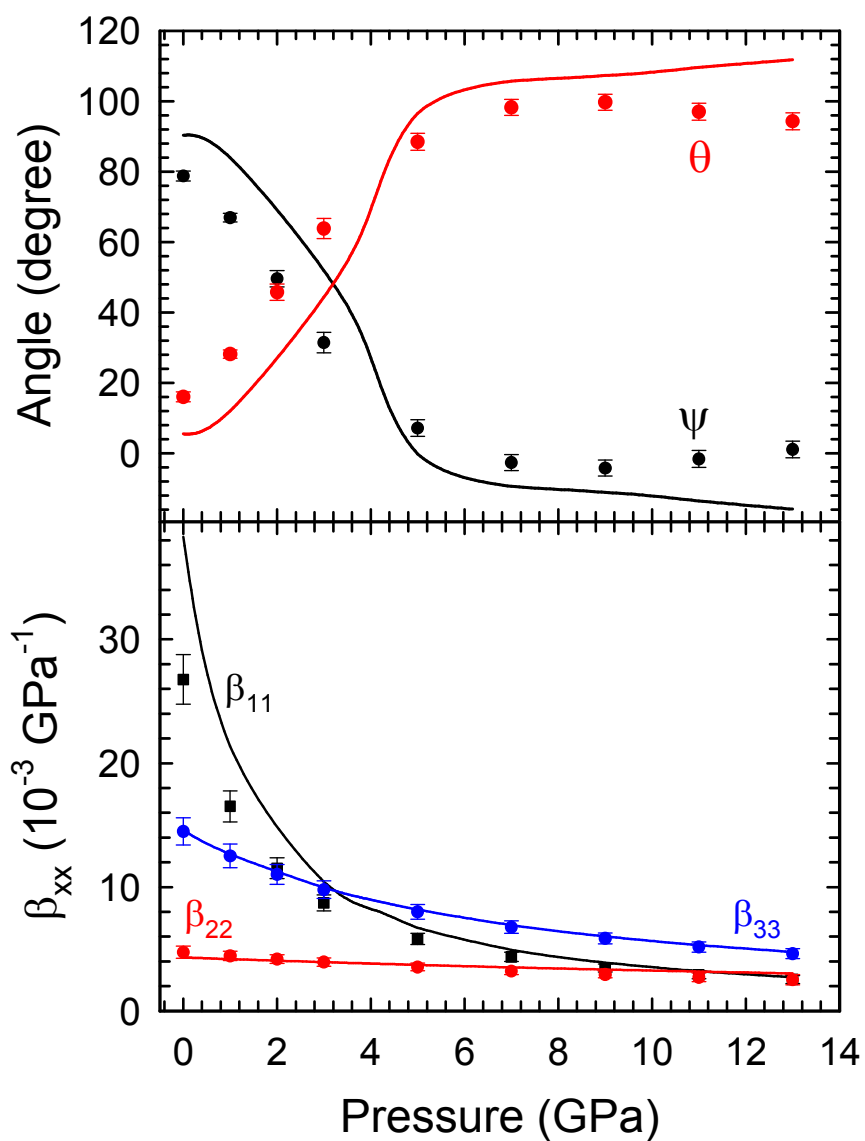
Figure S4. (a) Angle of maximum compressibility ψ relative to the *c*-axis (from *c* to *a*) or equivalently θ relative to the *a*-axis (from *a* to *c*). (b) β_{xx} coefficients of the compressibility tensor that indicates the compressibility along the crystallographic axis. Solid lines represent the *ab initio* calculations and symbols data obtained from our experiments.
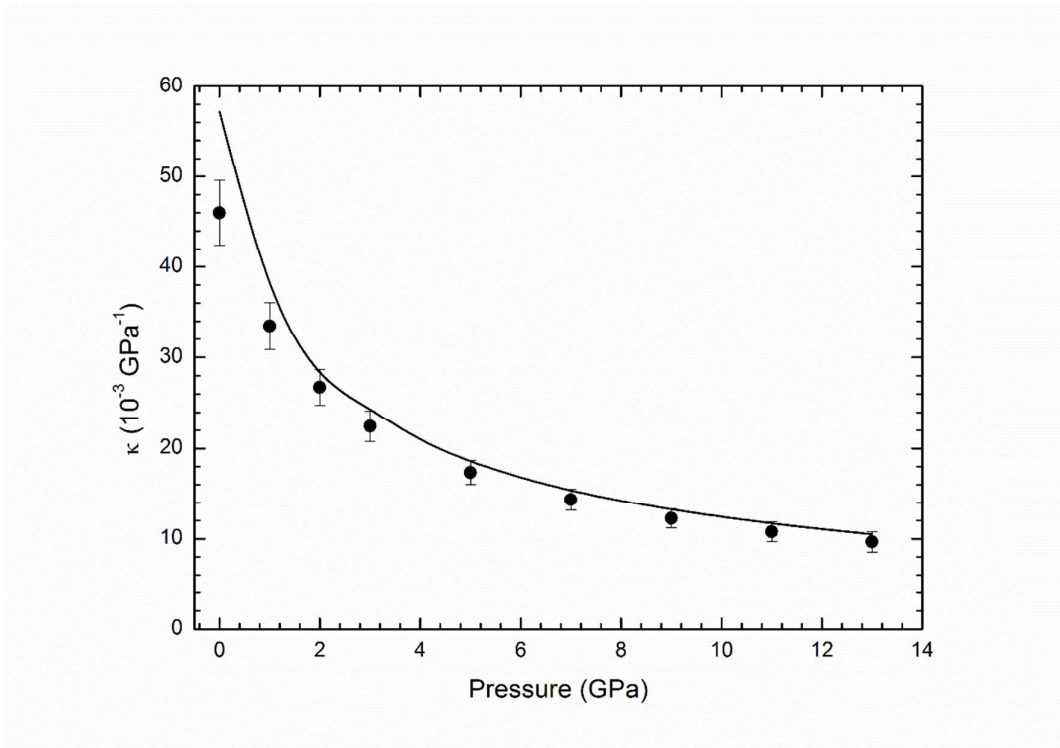
Figure S5. Experimental (symbols) and theoretical (curve) pressure dependence of the volume compressibility as obtained from the trace of the experimental and theoretical compressibility tensors at different pressures.

Pressure dependence of atomic coordinates and interatomic distances
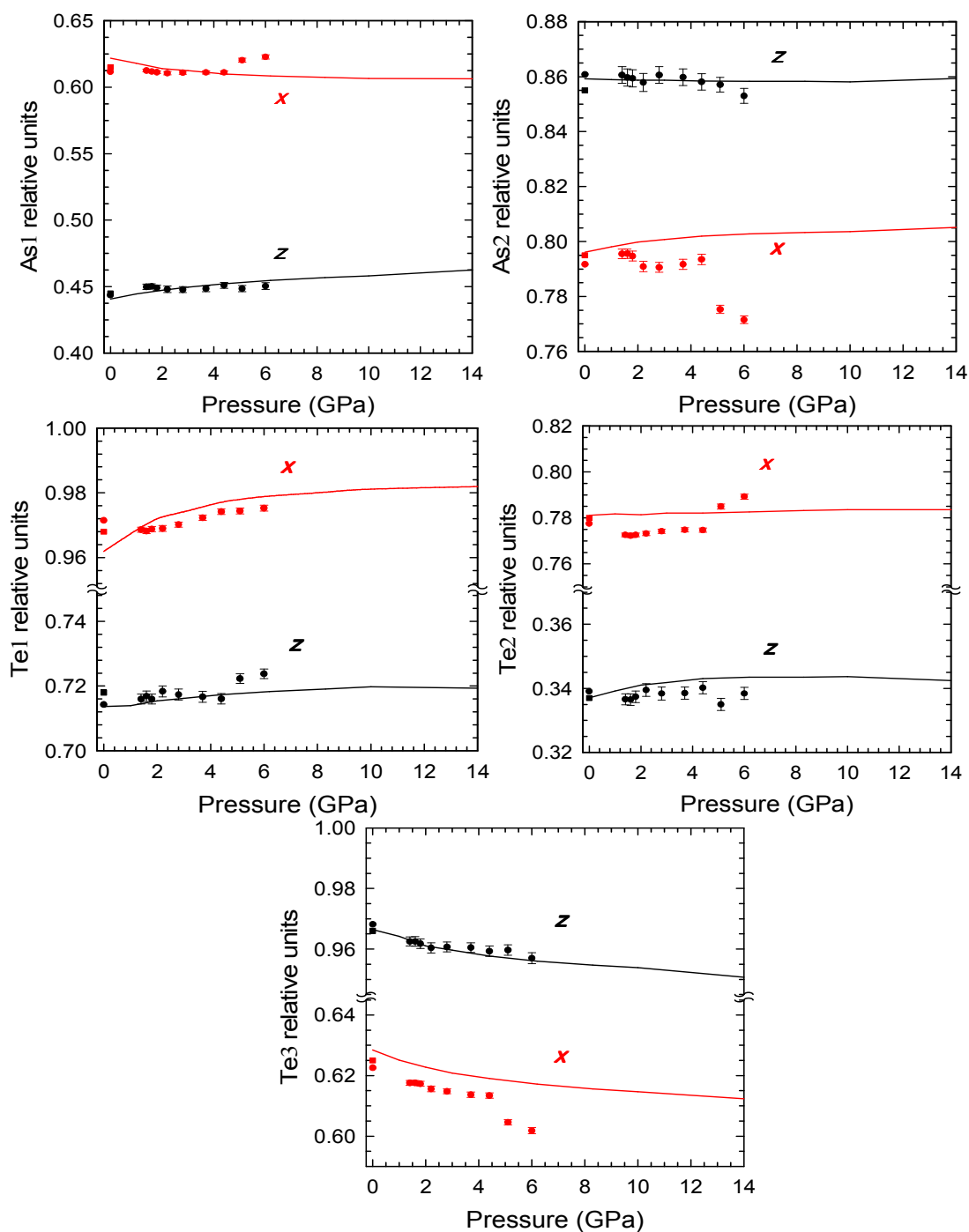
Figure S6. Pressure dependence of the experimental (symbols) and theoretical (lines) As1, As2, Te1, Te2 and Te3 x and z coordinates in α-As$_2$Te$_3$. Squares correspond to data at ambient pressure taken from Ref. 10.
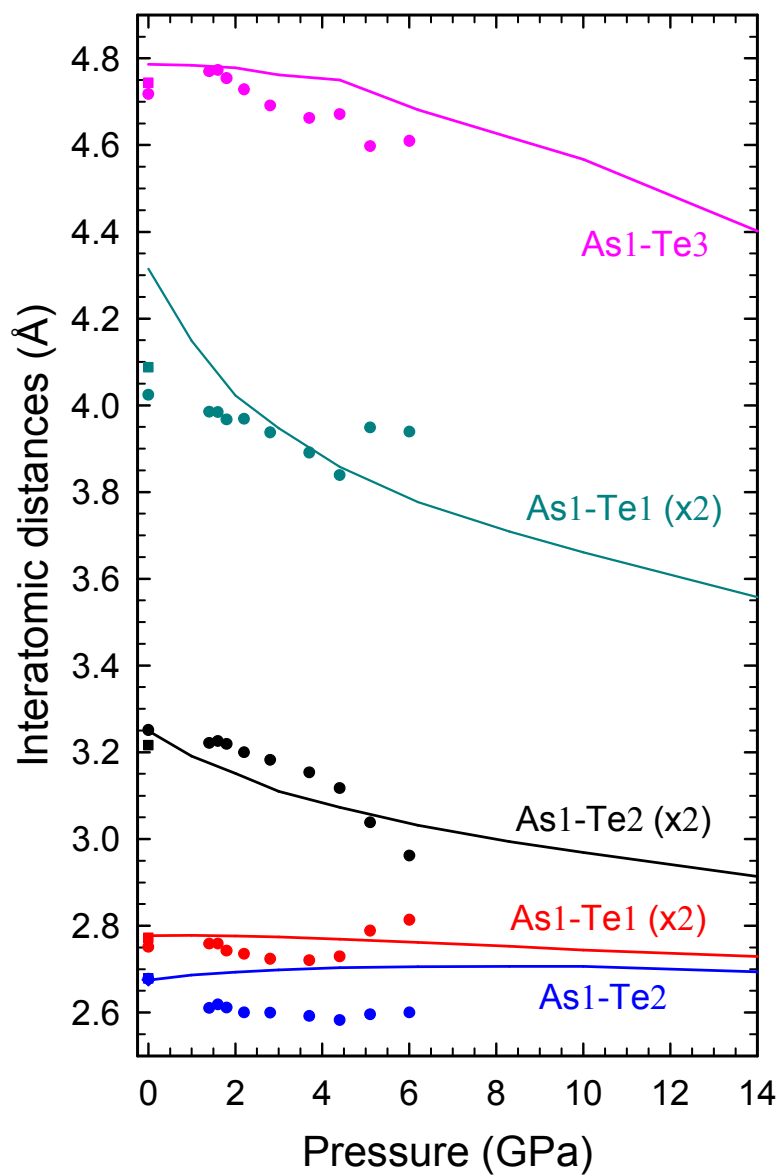
Figure S7. Pressure dependence of the experimental (symbols) and theoretical (lines) As1-Te distances. Squares correspond to data at ambient pressure taken from Ref. 10.
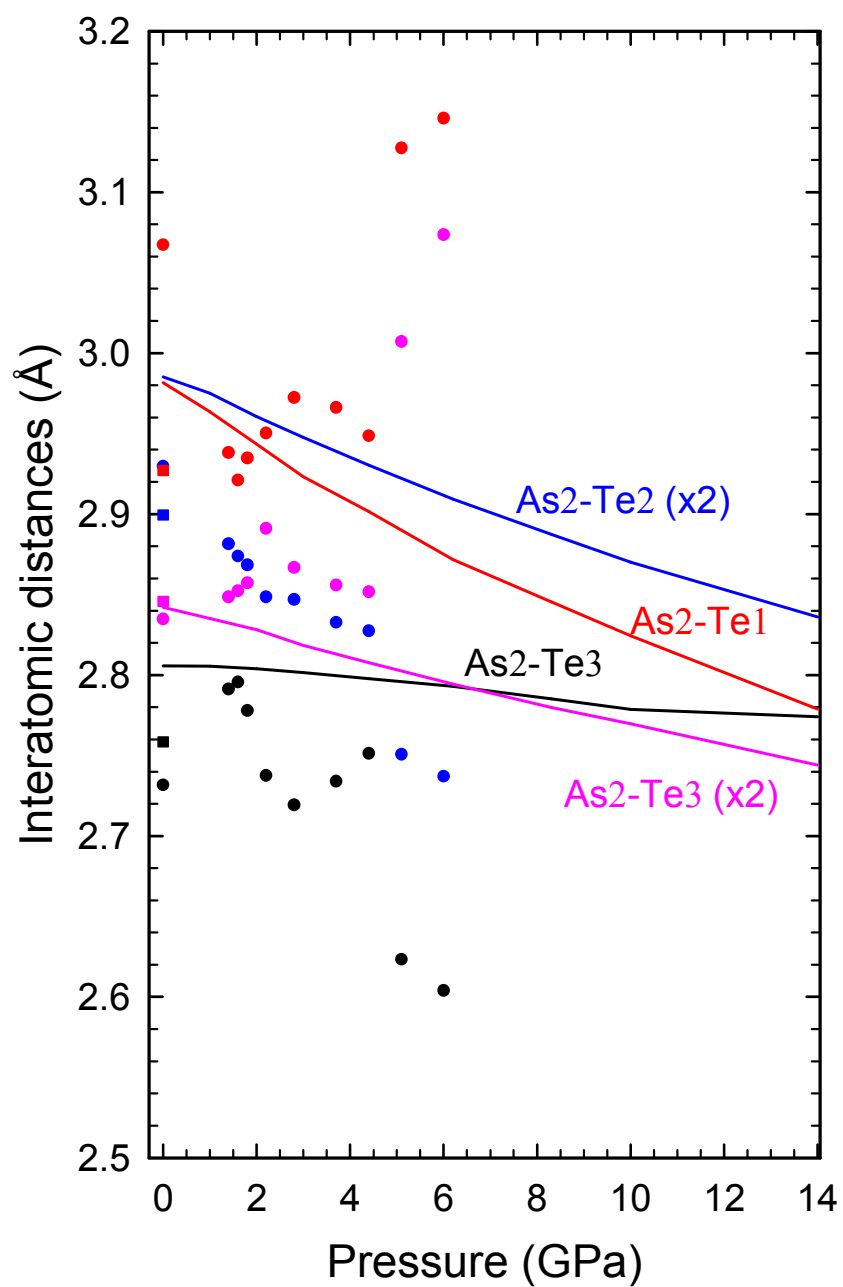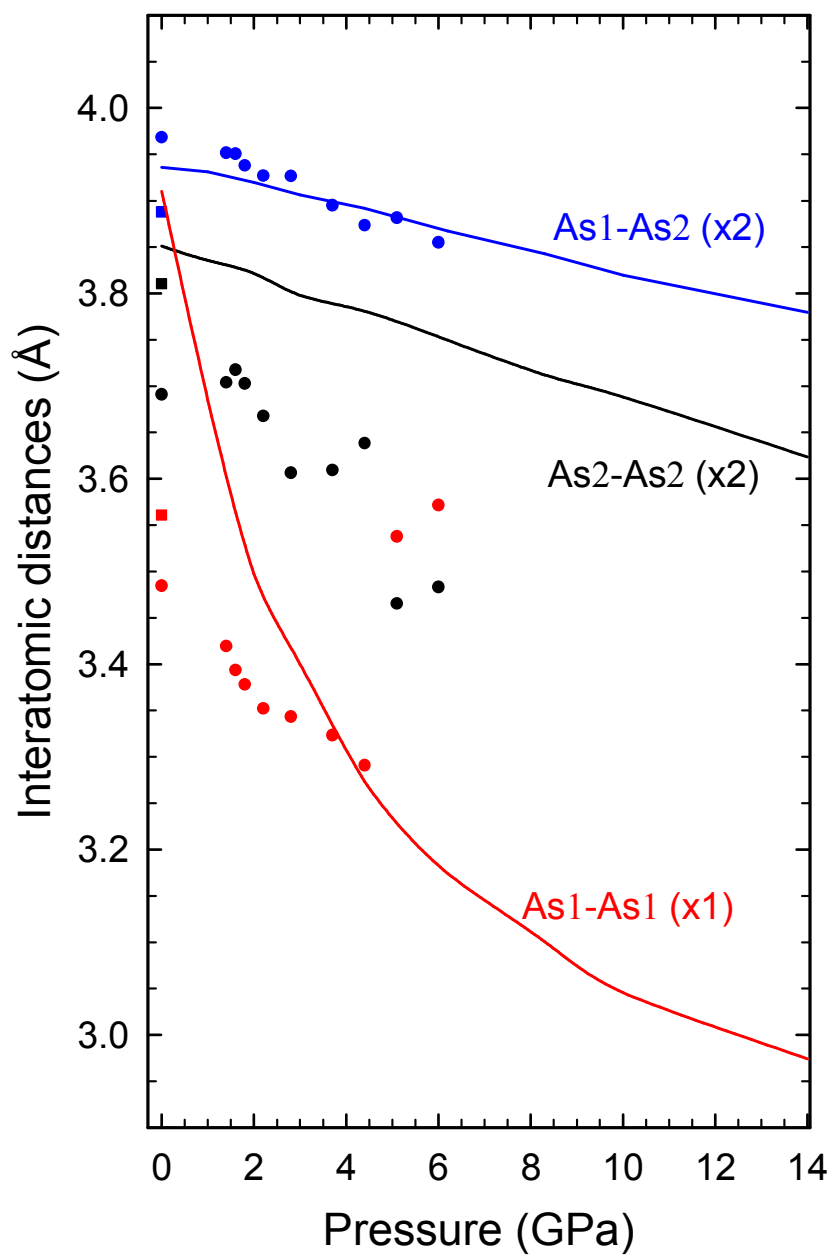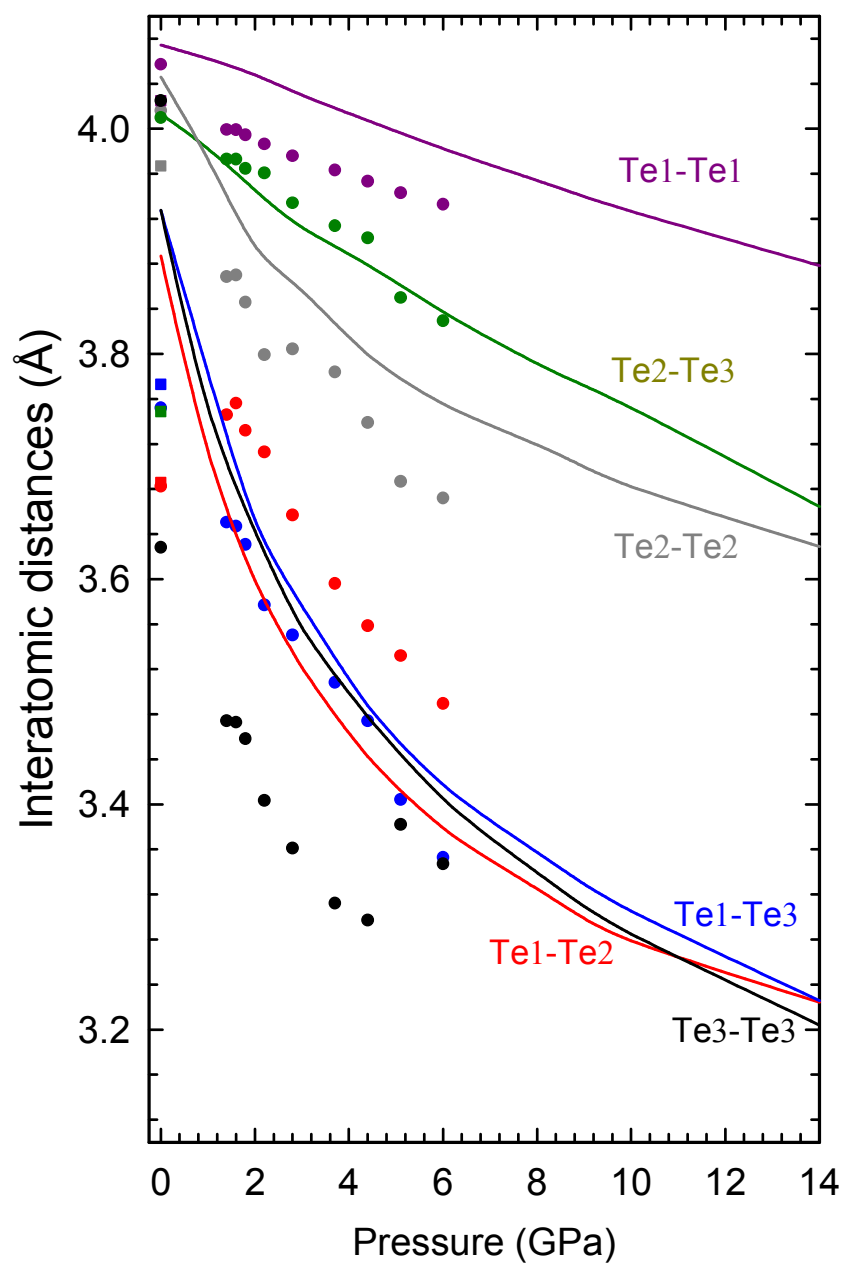
Figure S8. Pressure dependence of the experimental (symbols) and theoretical (lines)

As2-Te distances. Squares correspond to data at ambient pressure taken from Ref. 10.
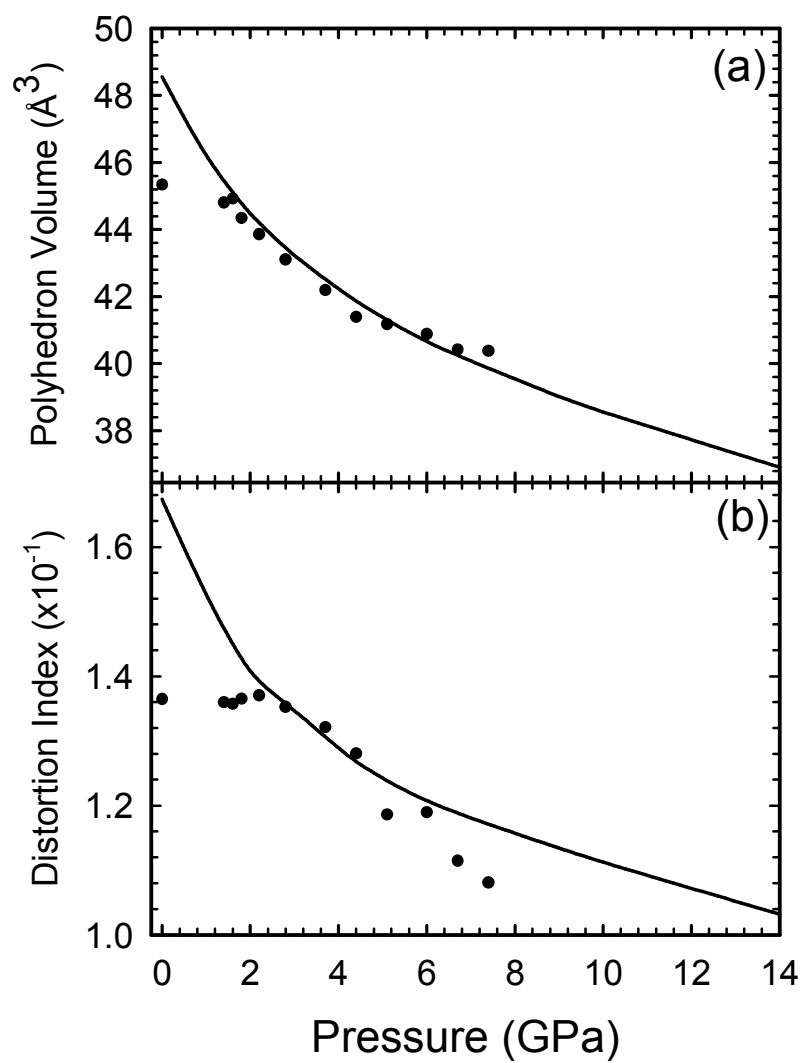
Figure S9. Pressure dependence of the experimental (symbols) and theoretical (lines) As-As distances. Squares correspond to data at ambient pressure taken from Ref. 10.

Figure S10. Pressure dependence of the experimental (symbols) and theoretical (lines)

Te-Te distances. Squares correspond to data at ambient pressure taken from Ref. 10.

Figure S11. Pressure dependence of the experimental (symbols) and theoretical (lines) volume (a) and distortion index (b) of the As1 polyhedron.
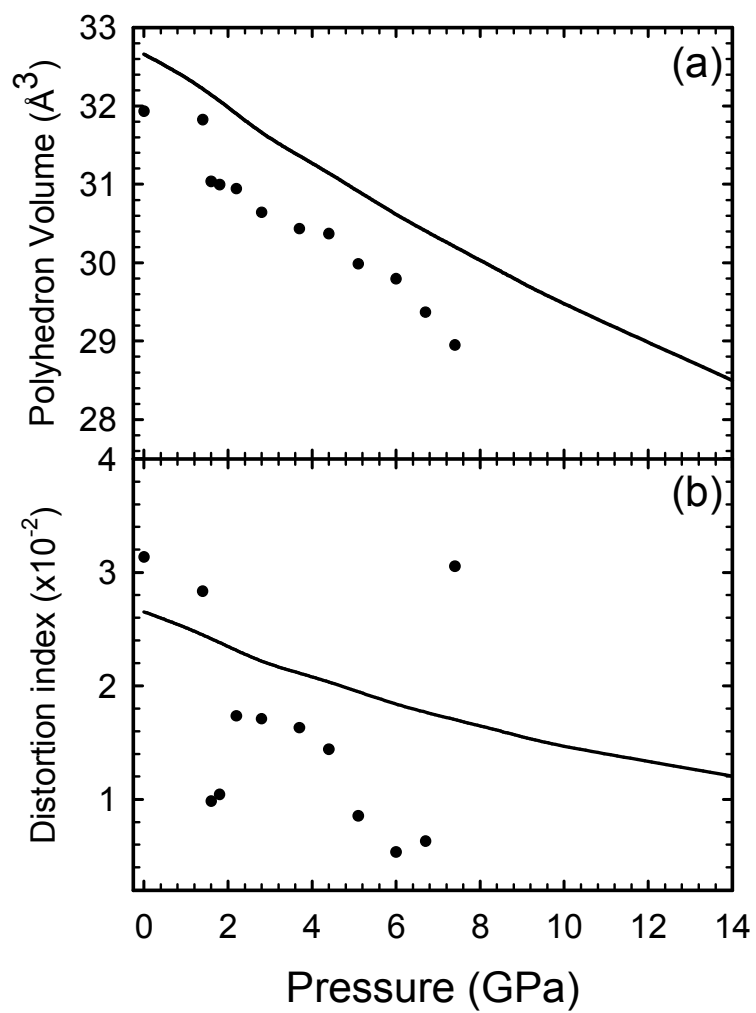
Figure S12. Pressure dependence of the experimental (symbols) and theoretical (lines) volume (a) and distortion index (b) of the As2 polyhedron.

Comparison of the structure of α-As₂Te₃ and its pressure behavior with other related group-15 sesquichalcogenides

It is interesting to compare the structure of α-As$_2$Te$_3$ and its pressure behavior with that of other group-15 sesquioxides and sesquichalcogenides in order to understand the role played by the As LEP in the structure of α-As$_2$Te$_3$. **Table S3** summarizes the experimental and theoretical BM-EoS of α-As$_2$Te$_3$, α-Sb$_2$Te$_3$, α-Bi$_2$Te$_3$ and orthorhombic Sb$_2$Se$_3$. As observed, the bulk modulus of α-As$_2$Te$_3$ is smaller than those of α-Sb$_2$Te$_3$ and α-Bi$_2$Te$_3$. This result is in good agreement with the larger activity of the LEP in As than in Sb and Bi tellurides and how this activity favors open structures with a large compressibility. In this way, it is easy to understand that the increase of the cation LEP activity in the series Bi-Sb-As explains that distorted structures caused by the cation LEP are present in Bi$_2$X$_3$ (X= O, S), Sb$_2$X$_3$ (X= O, S, Se) and As$_2$X$_3$ (X= O, S, Se, Te) since cation LEP activity is different for different anions [31]. The comparison of compounds with the same anion, shows that the volume per unit formula rises when the atomic number of the cation increases, as expected by the increase of the cationic radius size. However, the LEP effect softens this increase allowing a small increment of the initial volume of α-As$_2$Te$_3$ compared with that observed in α-Sb$_2$Te$_3$. On the other hand, the bulk modulus of α-As$_2$Te$_3$ is similar to that of Sb$_2$Se$_3$.

It is also worthy to compare the compressibility of the different axes in these compounds (see **Table S4**). The experimental compressibility of the *a*-axis at room pressure in α-As$_2$Te$_3$ (26.8(2)·10^{-3} GPa^{-1}) can be compared to that of the *c*-axis in α-Sb$_2$Te$_3$ (around 21.2·10^{-3} GPa^{-1}) [85] and α-Bi$_2$Te$_3$ (around 15.2·10^{-3} GPa^{-1}) [89] since layers are mainly stacked along these directions in the different compounds. As observed, the interlayer compressibility of α-As$_2$Te$_3$ is larger than of α-Sb$_2$Te$_3$ and α-Bi$_2$Te$_3$. Again, this result is in good agreement with the larger Te-Te interlayer distance observed in As telluride than in Sb and Bi tellurides as expected by the larger cation LEP activity of As than of Sb and Bi for the same anion. On the contrary, the intralayer compressibility at room pressure, which is mainly that of *b*-axis in α-As$_2$Te$_3$ (4.7(5)·10^{-3} GPa^{-1}) and that of *a*-axis in α-Sb$_2$Te$_3$ (6.2·10^{-3} GPa^{-1}) [19] and α-Bi$_2$Te$_3$ (8.4·10^{-3} GPa^{-1}) [24] are smaller than those of the other axes in the three compounds, as expected for the intralayer strong covalent *A*-Te (*A*= As, Sb, Bi) bonds.

An even closer comparison of axial compressibilities can be performed between α-As$_2$Te$_3$ and Sb$_2$Se$_3$ since the latter compound crystallizes in an orthorhombic layered

structure (*Pnma* space group) isostructural to Sb_2S_3 and Bi_2S_3 and with similar tendency than α-As_2Te_3 to form needles extended along the *b*-axis which are weakly linked to form extended layers. The structure of Sb_2Se_3 is more distorted than that of α-As_2Te_3 and has also two independent cations, Sb1 and Sb2. At room pressure, both cations are bonded to three Se atoms with short bonds (< 2.7 Å) and to four additional Se atoms with longer bonds (> 3.0 Å), giving rise to an apparent sevenfold coordination. Actually, the coordination at ambient pressure is much smaller. The shortest bonds give rise to distorted trigonal Sb1Se3 units and tetragonal Sb2Se5 pyramids, thus resulting in Sb1Se3E tetrahedra and Sb2Se5E octahedra (where E indicates the LEP of both Sb atoms) of quasi-fourfold and quasi-sixfold coordination, respectively. Similarly to Sb_2Se_3, the polyhedral units of α-As_2Te_3 could be described as As1Te5E octahedra and As2Te6 octahedra. From this perspective, it is observed that the cation LEP is active in both polyhedral units of Sb2Se3, but only in one polyhedral unit of α-As_2Te_3; i.e., the LEP activity of Sb in Sb_2Se_3 is larger than that of As in α-As_2Te_3. This different LEP activity is a consequence that the cation LEP activity depends on the anion and increases for lighter anions as already reported elsewhere [31].

Due to the larger cation LEP activity in Sb_2Se_3 than in α-As_2Te_3, the zigzag layers in Sb_2Se_3 are cut along the *c*-axis [32]. Inside the needles extended along the *b*-axis, intralayer Sb-Se distances are around 2.67 Å; a value similar to that of most intralayer As-Te bonds (**Figs. S6 and S7**). These needles are separated from adjacent ones in a zigzag way by intermediate primary and secondary interchain distances (around 3.1 Å) mainly along the *c*-axis. Finally, the layers formed by linked chains along *b* and *c* axes pile up along the *a*-axis with large distances between layers (around 3.7 Å) [32]. In this way, the structure of Sb_2Se_3 results in a *b* lattice parameter around 4 Å, similar to that of α-As_2Te_3, while *a* and *c* lattice parameters are around 11.8 Å and 11.6 Å, respectively. The compresibilities of *a*, *b* and *c* axes in Sb_2Se_3 at room pressure are around $13.6 \cdot 10^{-3}$, $5.0 \cdot 10^{-3}$ and $9.3 \cdot 10^{-3}$ GPa^{-1} [30] so they clearly scale with the lattice parameter values and with the Sb-Se distances along the different directions. This situation is the same already described for α-As_2Te_3 where the compressibility of the *a*, *b* and *c* axes at room pressure scale with the lattice parameters and with the interlayer Te-Te distance (around 3.8 Å), with the intralayer As2-Te distances (around 2.8 Å), and with the intralayer As1-Te distance (around 3.2 Å). The largest difference in axial compressibilities between α-As_2Te_3 and Sb_2Se_3 occurs along the *a*-axis. This result

must be ascribed to the different compressibility of van der Waals interlayer Te-Te distances than Se-Se distances since all three tellurides show larger interlayer compressibilities than the selenide Sb_2Se_3.

In summary, the structure of α-As_2Te_3 can be understood as intermediate between that of α-Sb_2Te_3 and Sb_2Se_3 in good agreement with what is expected from the activity of cation LEP in group-15 sesquichalcogenides.

Compound	V_0 (Å³)	B_0	B_0'	Character
α-As₂Te₃	144.8	24	7.9	Exp[a]
	143.0	26	9.0	Exp[b]
	143.0	33	4.0(fixed)	Exp[b]
	142.6	38.4	4.0(fixed)	Exp[c]
	150.8	19.7	8.1	The[a]
	138.4	42.7		The[d]
α-Sb₂Te₃	159.7	40	4 (fixed)	Exp[e]
	159.7	30.2	9.4	Exp[f]
		45	4 (fixed)	Exp[g]
	159.9	36.1	6.2	Exp[h]
	157.5	54.7	4	Exp[i]
	158.1	41.0	5.2	The[j]
	159.9	33.1		The[k]
α-Bi₂Te₃	169.2	56.2	2.1	Exp[f]
		21.9*	17.1	Exp[l]
		38.2**	4.6	
	168.5	28.1*	13.8	Exp[m]
	168.5	36.3**	5.5	
	170.0	46.3	3.6	Exp[n]
		50.1	3.0	Exp[o]
	166.7	41.6	4.68	The[p]
	168.8	28.1		The[q]
		40.3		The[r]
Sb₂Se₃	136.4	30	6.1	Exp[q]

[a] This work, [b] Ref. 13, [c] Ref. 14, [d] Ref. 15, [e] Ref. 16, [f] Ref. 17, [g] Ref. 18, [h] Ref. 19, [i] Ref. 20, [j] Ref. 21, [k] Ref. 22, [l] Ref. 23, [m] Ref. 24, [n] Ref. 25, [o] Ref. 26, [p] Ref. 27, [q] Ref. 28, [r] Ref. 29, [q] Ref. 30. * Values below 3 GPa. ** Values above 3 GPa.

Table S3. Experimental (Exp) and theoretical DFT-GGA (The) parameters of the BM-EoS of α-As₂Te₃, α-Sb₂Te₃, α-Bi₂Te₃ and Sb₂Se₃ at ambient pressure. Volumes per formula unit are taken for comparison of the different compounds.

Compound	a	χ_a	B	χ_b	c	χ_c
α-As$_2$Te$_3$[a]	14.55	26.8	4.03	4.7	9.96	14.5
Sb$_2$Se$_3$[b]	11.80	13.6	3.98	5.0	11.60	9.3
α-Sb$_2$Te$_3$[c]	4.27	6.2	4.27	6.2	15.19	21.2
α-Bi$_2$Te$_3$[d]	4.38	8.4	4.38	8.4	15.18	15.2

[a] This work, [b] Ref. 30, [c] Ref. 19, [d] Ref. 24.

Table S4. Lattice parameters (in Å) and compressibilities (in 10^{-3} GPa^{-1}) of α-As$_2$Te$_3$, α-Sb$_2$Te$_3$, α-Bi$_2$Te$_3$ and Sb$_2$Se$_3$ at ambient pressure. Values with same shadow color correspond to distances and compressibilities to be compared. Note that c lattice parameter of α-Sb$_2$Te$_3$ and α-Bi$_2$Te$_3$ has been divided by 2 because there are two times more layers along the unit cell of these compounds than along the a-axis of α-As$_2$Te$_3$ and Sb$_2$Se$_3$.

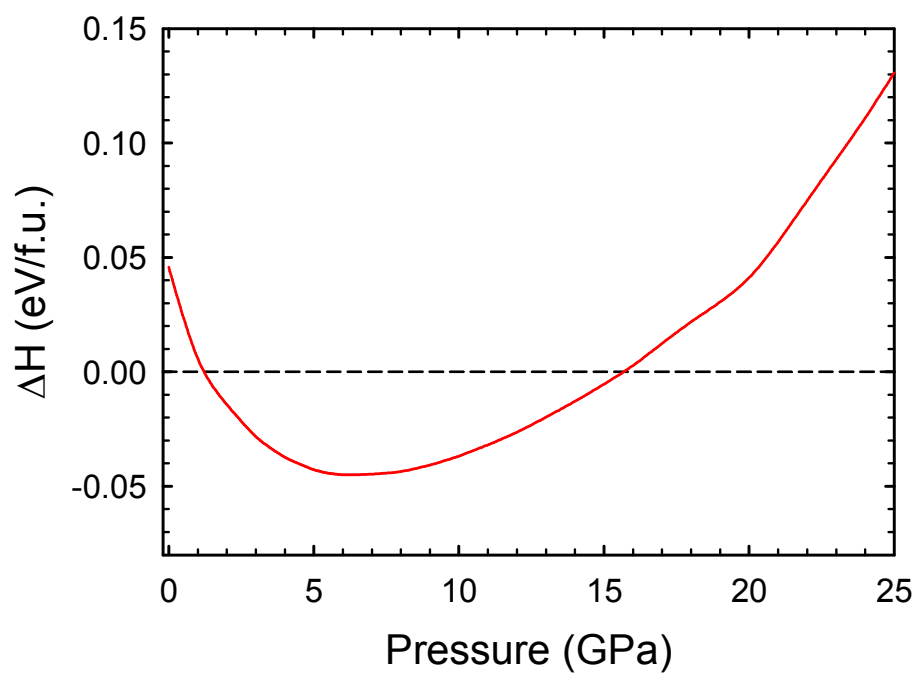**Ab-initio calculations of enthalpy vs pressure**

Figure S13. Enthalpy difference curves of the α (black dashed line) and β (red solid line) phases as a function of pressure with respect to the α-phase which has been taken as a reference.

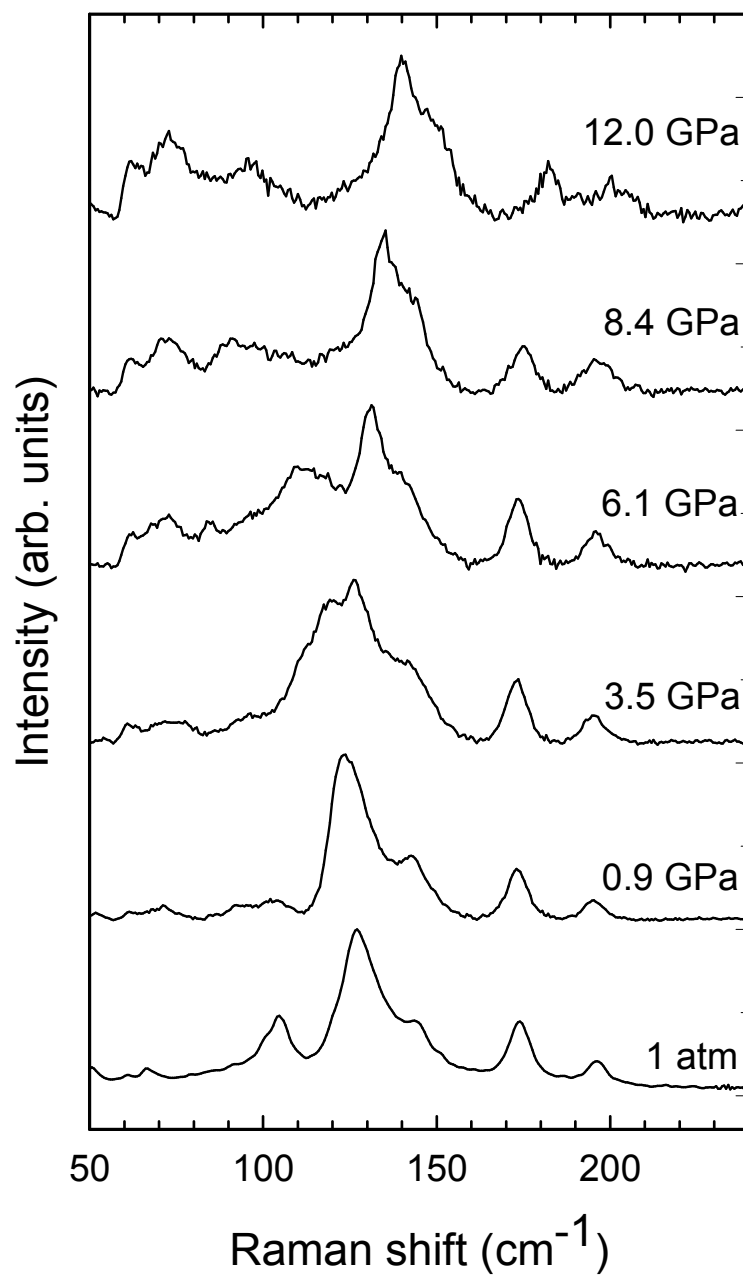**Vibrational properties of α-As₂Te₃ at high pressures**

Figure S14. Room-temperature Raman spectra of α-As₂Te₃ at selected pressures under non-hydrostatic conditions.
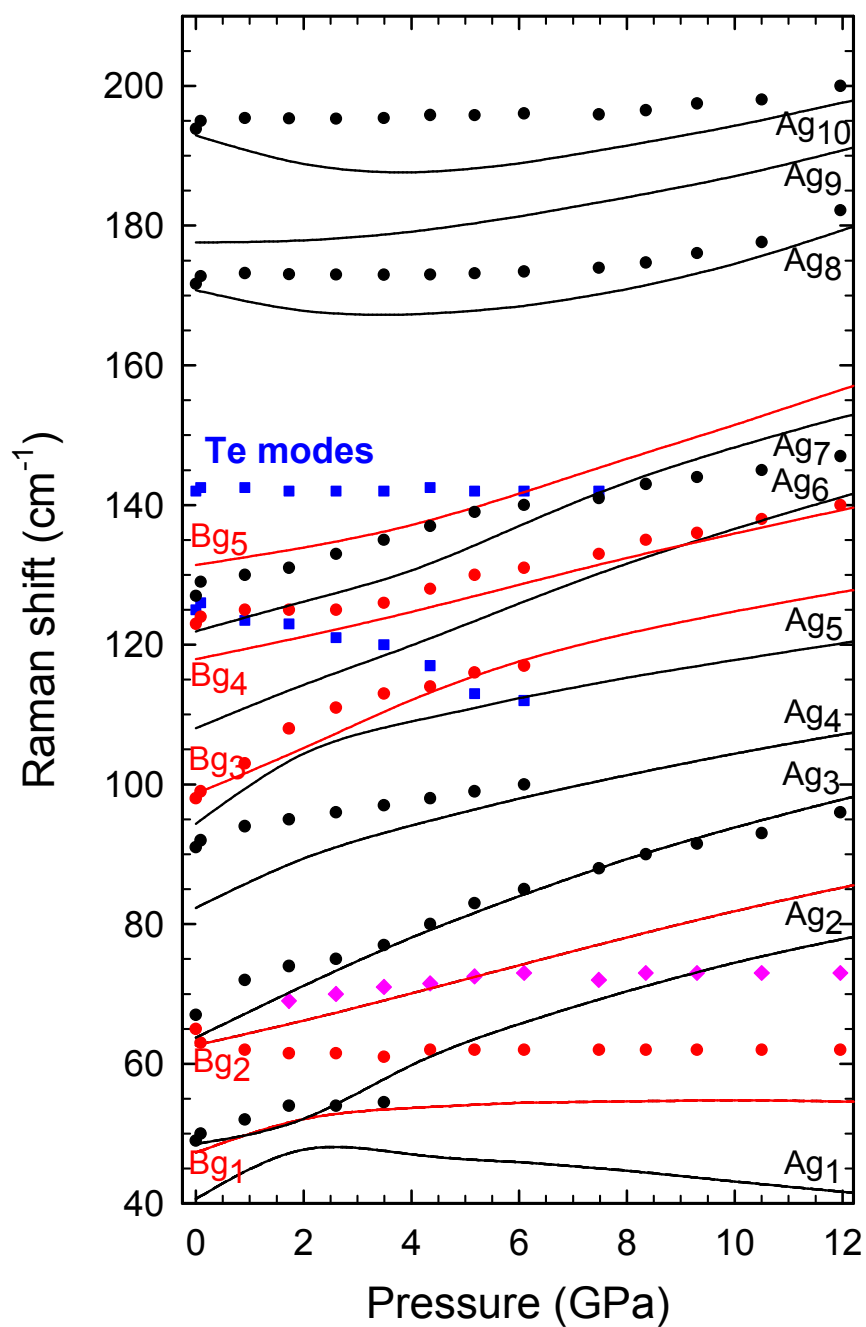
Figure S15. Experimental (symbols) and theoretical (lines) pressure dependence of the Raman-mode frequencies of α-As₂Te₃ under non-hydrostatic conditions. Different colors represent Raman-active modes of different symmetries.
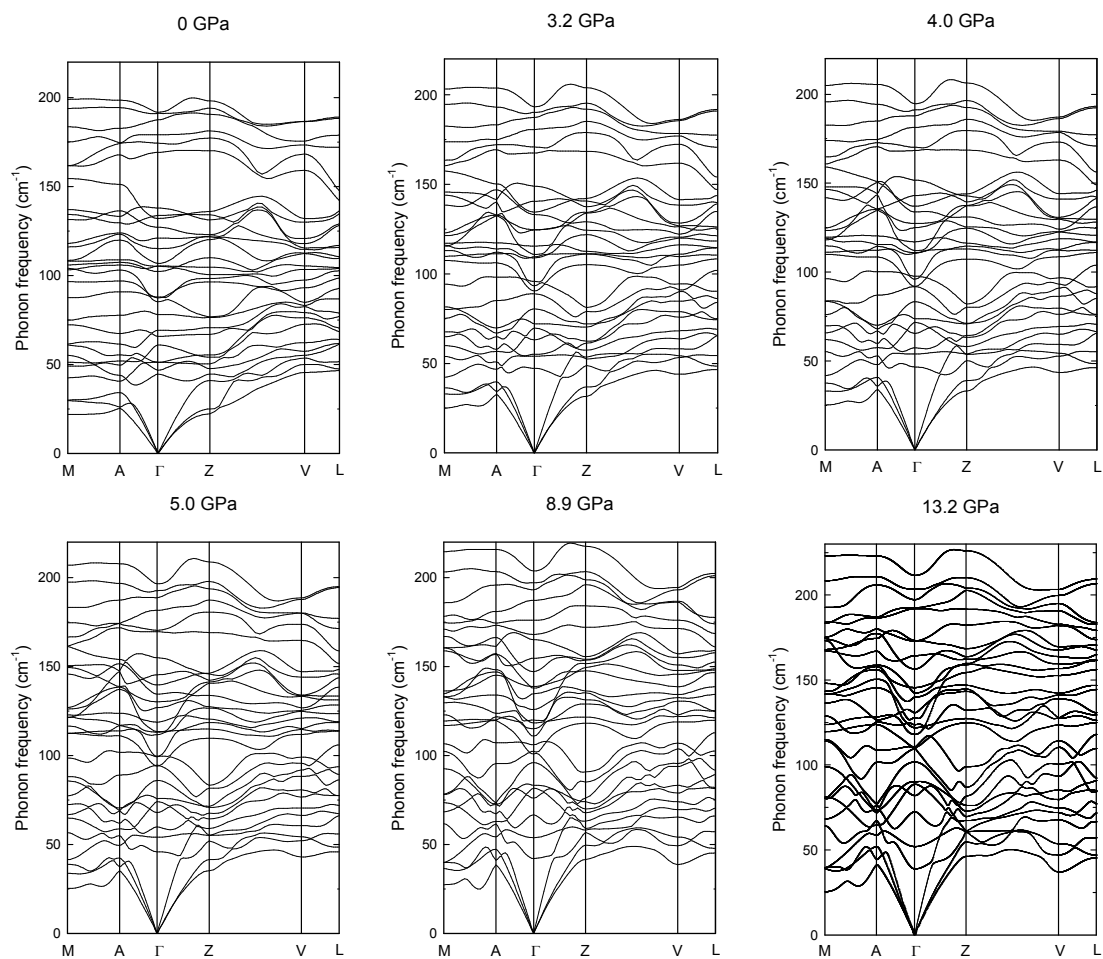
Figure S16. Theoretical phonon dispersion curves of α-As$_2$Te$_3$ at different pressures.

No soft phonon mode is observed either at Γ or at any other point of the Brillouin zone.

References

(1) Mendoza-Galván, A.; García-García, E.; Vorobiev, Y.V.; González-Hernández, J. Structural, Optical and Electrical Characterization of Amorphous SexTe1-x Thin Film Alloys. Microelectron. Eng. **2000**, *51-52*, 677-687.

(2) Usuki, T.; Saitoh, K.; Endo, M.; Uemura, O. Short-Range Order of Amorphous and Liquid As-Te-I System, J. Non-Cryst. Solids **1996**, *205-207*, 184-188.

(3) Tverjanovich, A.; Rodionov, K.; Bychkov, E. Raman Spectroscopy of Glasses in the As-Te System. *J. Solid State Chem.* **2012**, *190*, 271-276.

(4) Alekberov, R.I.; Mekhtiyeva, S.I.; Isayeva, G.A.; Isayev, A.I. Raman Scattering in As-Se-S and As-Se-Te Chalcogenide Vitreous Semiconductors, *Semic.* **2014**, *48*, 800-803.

(5) Taylor, P.C.; Bishop, S.G.; Mitchell, D.L. Infrared Properties of AsxTe1-x glasses, Solid State Commun. **1975**, *16*, 167-170.

(6) Lukic, S.R.; Petrovic, D.M.; Skuban, S.J.; Radonjic, Lj.; Cvejic, Z. Formation of Complex Structural Units and Structure of As-S-Se-Te-I Glasses. *J. Opt. Adv. Mat.* **2003**, *5*, 1223-12229.

(7) Zallen, R.; Slade, M.L.; Ward, A.T. Lattice Vibrations and Interlayer Interactions in Crystalline As_2S_3 and As_2Se_3. *Phys. Rev. B* **1971**, *3*, 4257-4273.

(8) Canepa P.; Hanson, R. M.; Ugliengo, P.; Alfredsson, M. J-ICE: a New Jmol Interface for Handling and Visualizing Crystallographic and Electronic Properties. *J. Appl. Cryst.* **2011**, *44*, 225-229.

(9) Pereira, A. L. J.; Gomis, O.; Sans, J. A.; Pellicer-Porres, J.; Manjón, F. J.; Beltrán, A.; Rodríguez-Hernández, P.; Muñoz, A. Pressure Effects on the Vibrational Properties

of α-Bi_2O_3: an Experimental and Theoretical Study. J. Phys.: Condens. Matter **2014**, *26*, 225401.

(10) Carron, G.J. The Crystal Structure and Powder Data for Arsenic Telluride. *Acta Cryst.* **1963**, *16*, 338-343.

(11) Haussühl, S. Physical Properties of Crystals. An Introduction, Wiley-VCH, Weinheim, 2007.

(12) Angel, R. J. http://www.rossangel.com/text_strain.htm

(13) Zhao, J.G.; Yang, L.X.; Yu, Z.H.; Wang, Y.; Li, C.Y.; Yang, K.; Liu, Z.G.; Wang, Y. Structural Phase Transitions and Metallized Phenomena in Arsenic Telluride under High Pressure. *Inorg. Chem.* **2016**, *55*, 3907.

(14) Zhang, Y.H.; Ma, Y.M.; Geng, A.H.; Zhu, C.Y.; Liu, G.T.; Tao, Q.; Li, F.F.; Wang, Q.L.; Li, Y.; Wang, X. et al. Pressure-Induced Electronic Phase Transitions of α-As_2Te_3. *J. Alloys Comp.* **2016**, *685*, 551-558.

(15) Deng, H. Theoretical Prediction of the Structural, Electronic, Mechanical and Thermodynamic Properties of the Binary α-As_2Te_3 and β-As_2Te_3. *J. Alloys and Comp.* **2015**, *656*, 695-701.

(16) Sakai, N.; Fritzsche, H. Semiconductor-Metal and Superconducting Transitions Induced by Pressure in Amorphous As_2Te_3. *Phys. Rev. B* **1977**, *15*, 973-978.

(17) Jacobsen, M.K.; Kumar, R.S.; Cornelius, A.L.; Sinogeiken, S.V.; Nicol, M.F. High Pressure X-Ray Diffraction Studies of $Bi_{2-x}Sb_xTe_3$ ($x = 0,1,2$). *AIP Conf. Proc.* **2007**, *955*, 171-174.

(18) Zhao, J.G.; Liu, H.Z.; Ehm, L.; Chen, Z. Q.; Sinogeikin, S.; Zhao, Y.S.; Gu, G. Pressure-Induced Disordered Substitution Alloy in Sb_2Te_3. *Inorg. Chem.* **2011**, *50*, 11291-11293.

(19) Souza, S.M.; Poffo, C.M.; Triches, D.M.; de Lima, J.C.; Grandi, T.A.; Polian, A.; Gauthier, M. High Pressure Monoclinic Phases of Sb_2Te_3. *Physica B* **2012**, *407*, 3781-3789.

(20) Ma, Y.M.; Liu, G.T.; Zhu, P.W.; Wang, H.; Wang, X.; Cui, Q.L.; Liu, J.; Ma, Y.M. Determinations of the High-Pressure Crystal Structures of Sb_2Te_3. *J. Phys: Condens. Matter* **2012**, *24*, 475403.

(21) Gomis, O.; Vilaplana, R.; Manjón, F.J.; Rodríguez-Hernández, P.; Pérez-González, E.; Muñoz, A.; Drasar, C.; Kucek, V. Lattice Dynamics of Sb_2Te_3 at High Pressures. *Phys. Rev. B* **2011**, *84*, 174305.

(22) Zhang, H.Y.; Cheng, Y.; Tang, M.; Chen, X.R. Ji, G.F. First-Principles Study of Structural, Elastic, Electronic and Thermodynamic Properties of Topological Insulator Sb_2Te_3 under Pressure. *Comp. Mat. Sci.* **2015**, *96*, 342-347.

(23) Nakayama, A.; Einaga, M.; Tanabe, Y.; Nakano, S.; Ishikawa, F.; Yamada, Y. Structural Phase Transition in Bi_2Te_3 under High Pressure. *High Pressure Res.* **2009**, *29*, 245-249.

(24) Polian, A.; Gauthier, M.; Souza, S.M.; Triches, D.M.; Cardoso de Lima, J.; Grandi, T. A. Two-Dimensional Pressure-Induced Electronic Topological Transition in Bi_2Te_3. *Phys. Rev. B* **2011**, *83*, 113106.

(25) Zhu, L.; Wang, H.; Wang, Y.; Lv, J.; Ma, Y.; Cui, Q.; Ma, Y.; Zou, G. Substitutional Alloy of Bi and Te at High Pressure. *Phys. Rev. Lett.* **2011**, *106*, 145501.

(26) Einaga, M.; Ohmura, A.; Nakayama, A.; Ishikawa, F.; Yamada, Y.; Nakano, S. Pressure-Induced Phase Transition of Bi_2Te_3 to a bcc Structure. Phys. Rev. B **2011**, *83*, 092102.

(27) Vilaplana, R.; Gomis, O.; Manjón, F. J.; Segura, A.; Perez-González, E.; Rodríguez-Hernández, P.; Muñoz, A.; González, J.; Marín-Borras, V.; Muñoz-Sanjosé, V. et al. High-Pressure Vibrational and Optical Study of Bi_2Te_3. *Phys. Rev. B* **2011**, *84*, 104112.

(28) Ibarra-Hernández, W.; Verstraete, M. J.; Raty, J.-Y. Effect of Hydrostatic Pressure on the Thermoelectric Properties of Bi_2Te_3. *Phys. Rev. B* **2014**, *90*, 245204.

(29) Feng, S.; Li, S.M.; Fu, H.Z. First-Principle Calculation and Quasi-Harmonic Debye Model Prediction for Elastic and Thermodynamic Properties of Bi_2Te_3. *Comp. Mat. Sci.* **2014**, *82*, 45-49.

(30) Efthimiopoulos, I.; Zhang, J.M.; Kucway, M.; Park, C.; Ewing, R.C.; Wang, Y. Sb_2Se_3 under Pressure. *Sci. Rep.* **2013**, *3*, 2665.

(31) Walsh, A.; Payne, D.J.; Egdell, R.G.; Watson, G.W. Stereochemistry of Post-Transition Metal Oxides: Revision of the Classical Lone Pair Model. *Chem. Soc. Rev.* **2011**, *40*, 4455-4463.

(32) Deringer, V.L.; Stoffel, R.P.; Wuttig, M.; Dronskowski, R. Vibrational Properties and Bonding Nature of Sb_2Se_3 and their Implications for Chalcogenide Materials. *Chem. Sci.* **2015**, *6*, 5255-5262.